6 Fundamentals of Dusty Plasmas

André Melzer[⋆] *and John Goree*[†]

[⋆] Institut für Physik, Ernst-Moritz-Arndt-Universität Greifswald, Felix-Hausdorff-Str. 6, 17487 Greifswald, Germany
[†] Department of Physics and Astronomy, The University of Iowa, Iowa City, IA 52242, USA

6.1 Introduction

Dusty plasmas have opened up a completely new line of research in the field of plasma physics. In addition to electrons, ions, neutrals in "ordinary" plasmas, dusty plasmas contain massive particles of nanometer to micrometer size. Dusty plasmas are widespread in astrophysical situations like in the rings of Saturn, in cometary tails or in interstellar clouds [1, 2]. In technological processing plasmas dust particles grow from molecules in reactive gases to nanometer size particles [3, 4]. The removal of such plasma-grown particles is an essential issue in computer chip manufacturing. In contrast, materials with novel properties, such as solar cells with much improved efficiency, can be manufactured from thin films with incorporated dust particles.

A fascinating property of dusty plasmas is that the particles can arrange in ordered crystal-like structures, so-called plasma crystals [5, 6]. In the plasma, the particles acquire high negative charges of hundreds or thousands of elementary charges due to the inflow of electrons and ions. Then, the Coulomb interaction of neighboring particles by far exceeds their thermal energy: the system is strongly coupled. The spatial and time scales of the particle motion allow easy observation by video microscopy. Weak frictional damping ensures that the dynamics and kinetics of individual particles become observable. Thus, dusty plasmas enable the investigation of crystal structure, solid and liquid plasmas, phase transitions, waves and many more phenomena on the kinetic particle level.

Dusty plasmas are subject to a number of forces that are typically unimportant in usual plasmas. With a clever exploitation of these forces, the particles can be confined in a vast variety of configurations which allows to study the equilibrium and dynamics in dusty plasmas in different geometries.

Dusty plasmas have a number of physical concepts and similarities in common with non-neutral plasmas, like pure ion plasmas in Paul or Penning traps [7], as well as with colloidal suspensions [8, 9], where charged plastic particles are immersed in an aqueous solution. To stress the analogy to complex fluids or colloidal suspensions, the names "complex plasmas" or "colloidal plasmas" are also frequently used when referring to strongly coupled dusty plasmas.

In the following, we will summarize the fundamental properties of dusty plasmas starting with particle charging and the forces acting on the dust in a plasma. We will then describe experimental techniques in dusty plasmas before the weak and strong coupling effects are

discussed. Finally, the dispersion of various wave types in dusty plasmas are presented. In our description, we focus on experiments. Other aspects of dusty plasmas are described in recent reviews or monographs, e.g. [10, 11, 12].

6.2 Particle charging

When a particle of solid matter is immersed in plasma, it acquires an electric charge. This charge is, in many cases, the reason that the particle is interesting. It is therefore of great interest to know how large the charge is.

Ordinary plasmas consisting of only electrons and ions are complicated enough, but at least a physicist can trust that the charge of the constituents is known. For a dusty plasma, one cannot trust even that. In general, the charge on a particle of solid matter immersed in a plasma is an unknown parameter, which depends on the size of the particle and the plasma conditions. The charge is not a constant, but can fluctuate randomly, or in response to fluctuations in plasma parameters such as the electron density.

To estimate the charge of a particle, there are several theoretical models and some experimental methods as well. In general, none of them yields a result with perfect precision. Here we will consider theoretical models of charging, which in general are useful for estimating the charge with an accuracy of about a factor of two. These models will also be useful for gaining a conceptual understanding of how the charge varies with plasma parameters, and how it can vary in time.

The most common model is called the ”orbit-motion-limited” theory, which assumes collisionless ions, and this method will be reviewed here. Like other charging theories, this model is also useful for calculating the charge and potential of larger objects in a plasma, such as a spacecraft or a Langmuir probe.

Another model, intended for plasmas with collisional ions, is the ABR method [13]. Since dust is most commonly found in plasmas with an electron temperature T_{e} below 10 eV, the plasma is usually not fully ionized, so that ions collide with neutral gas molecules. If the mean-free-path for ion-neutral collisions is much longer than the screening length (Debye length) for electrons and ions in the plasma, then it is reasonable to ignore ion-neutral collisions, for the purpose of computing the charge. For laboratory conditions where the screening length is typically 1 mm or less, collisionality could be significant at pressures higher than about 100 Pa.

There are also some other models, often implemented numerically, which are mentioned briefly at the end of this section.

6.2.1 Orbital-motion limited theory

Most theories for predicting the charge of a dust particle in a plasma were originally developed to model electrostatic probes in plasmas. A dust particle is just a solid object immersed in plasma. One can view the dust particle as essentially a small probe, except that the dust particle has no wires connected to it. The starting point of these theories is a prediction of the electron and ion currents to the probe. The currents are termed ”orbit-limited” when the condition $a \ll \lambda_{\mathrm{D}} \ll \lambda_{\mathrm{mfp}}$ applies, where a is the particle radius, λ_{D} is the screening

or Debye length, and $\lambda_{\rm mfp}$ is a collisional mean-free-path between neutral gas atoms and either electrons or ions [14, 15]. In that case, the currents are calculated by assuming that the electrons and ions are collected if their collisionless orbits intersect the probe's surface. It is assumed that the currents are infinitely divisible; that is, the discrete nature of the electronic charge is ignored. The latter assumption must be reversed to account for the fluctuations on the particle, as shown later.

Analytic models including the OML model typically assume that the particle is spherical, and its surface is an equipotential. In this case, even if the particle is not made of a conductive material, it can be modeled as a capacitor. The charge Q is then related to the particle's surface potential ϕ_s, with respect to a plasma potential of zero, by

$$Q_{\rm d} = C\phi_s \quad , \tag{6.1}$$

where C is the capacitance of the particle in the plasma. For a spherical particle satisfying $a \ll \lambda_{\rm D}$, the capacitance is [16]

$$C = 4\pi\epsilon_0 a \quad . \tag{6.2}$$

If the particle is not made of a conducting material, and if it is positioned in an anisotropic plasma, especially a plasma with flowing ions, then its surface might not be an equipotential, and equations (6.1) and (6.2) will not be useful in computing an accurate value for the charge Q. For conditions with dielectric particles immersed in plasma with flowing ions, instead of using the OML model one can perform numerical simulations [17, 18, 19]. Here we will review only the OML model.

For the collection of Maxwellian electrons and ions, characterized by temperatures $T_{\rm e}$ and $T_{\rm i}$, the orbit-limited currents for an isolated spherical particle are [16]

$$\begin{aligned} I_{\rm e} &= I_{0\rm e}\exp(e\phi_{\rm s}/kT_{\rm e}) \qquad \phi_{\rm s} < 0 \\ I_{\rm e} &= I_{0\rm e}\,(1 + e\phi_{\rm s}/kT_{\rm e}) \qquad \phi_{\rm s} > 0 \\ I_{\rm i} &= I_{0\rm i}\exp(-q_{\rm i}\phi_{\rm s}/kT_{\rm i}) \qquad \phi_{\rm s} > 0 \\ I_{\rm i} &= I_{0\rm i}\,(1 - q_{\rm i}\phi_{\rm s}/kT_{\rm i}) \qquad \phi_{\rm s} < 0 \end{aligned} \tag{6.3}$$

Here $q_{\rm i} = z_{\rm i}e$ is the electronic charge of the ions. The coefficients $I_{0\rm e}$ and $I_{0\rm i}$ represent the current that is collected for $\phi_{\rm s} = 0$, and are given by

$$I_{0\alpha} = n_\alpha q_\alpha \sqrt{\frac{kT_\alpha}{m_\alpha}}\pi a^2 f_\alpha(u, v_{\rm th}) \quad , \tag{6.4}$$

where n_α is the number density of plasma species α. Here $f_\alpha(u, v_{\rm th})$ is a function that can be found in Eq. 4.4 of Ref. [16]; it is a rather complicated function of the thermal velocity $v_{\rm th} = (2kT_\alpha/m_\alpha)^{1/2}$ and the drift velocity u between the plasma and the particles. Simple expressions for f_α are available in the limiting cases of small and large drift velocities:

$$I_{0\alpha} = 4\pi a^2 n_\alpha q_\alpha \sqrt{\frac{kT_\alpha}{2\pi m_\alpha}} \qquad u/v_{\rm th} \ll 1 \tag{6.5}$$

$$I_{0\alpha} = \pi a^2 n_\alpha q_\alpha u \left(1 - \frac{2q_\alpha\phi_{\rm s}}{m_\alpha u^2}\right) \qquad u/v_{\rm th} \gg 1 \quad . \tag{6.6}$$

Now we need to compute the charge Q, based on these currents. Neglecting the discrete nature of the electron's charge, the currents are continuous quantities, and the dust particle's charge Q is allowed to vary smoothly, rather than in integer multiples of the electronic charge. A particle with zero charge that is immersed in plasma will gradually charge up, by collecting electron and ion currents, according to

$$\frac{dQ_{\mathrm{d}}}{dt} = \sum_{\alpha} I_{\alpha} \quad . \tag{6.7}$$

To find the equilibrium, one can set $dQ_{\mathrm{d}}/dt = 0$ in Eq. (6.7). This yields the steady-state potential ϕ_{fl} and steady-state charge $\langle Q_{\mathrm{d}} \rangle$,

$$\phi_{\mathrm{fl}} = \langle \phi_{\mathrm{s}} \rangle = K_{\phi} T_{\mathrm{e}} \tag{6.8}$$

$$\langle Q_{\mathrm{d}} \rangle / e = K_{\mathrm{Q}} a k T_{\mathrm{e}} \tag{6.9}$$

where the coefficients K_{ϕ} and K_{Q} are functions of $T_{\mathrm{i}}/T_{\mathrm{e}}$ and $m_{\mathrm{e}}/m_{\mathrm{e}}$, and the ion flow velocity, and they must be determined numerically. Useful values for these coefficients are listed in table 6.1 for cases with no ion flow.

The polarity of the dust particle's charge and surface potential will be negative if the particle does not emit electrons. That is so because electrons have a higher thermal velocity than ions. On the other hand, if the particle emits electrons due to impact of energetic electrons or ultraviolet photons (i.e., secondary electron emission or photoemission), the particle can charge positively. This condition occurs commonly in astrophysical and space plasmas, where the electron and ion densities are low and the currents collected from incident ions and electrons is small, but it is uncommon in laboratory plasmas.

Note that ϕ_{fl} is independent of the particle's size, but it depends on the plasma temperatures. On the other hand, the charge $\langle Q_{\mathrm{d}} \rangle$ is proportional to the particle's radius, $\langle Q_{\mathrm{d}} \rangle \propto a$. For example, a sphere in a non-flowing hydrogen plasma with $T_{\mathrm{e}} = T_{\mathrm{i}}$ has the Spitzer [20] potential $\phi_{\mathrm{fl}} = -2.50 k T_{\mathrm{e}}/e$.

As was mentioned earlier, the charge on a dust particle is not fixed, but it can fluctuate. The fluctuation can be in response to varying plasma conditions, for example. The charging time τ indicates how rapidly a particle's charge can vary, when plasma conditions vary. One way of defining a charging time is the ratio of the equilibrium charge and one of the currents, electron or ion, collected during equilibrium conditions. Another definition [21] assumes that hypothetically the particle has no charge and is suddenly immersed in a plasma with conditions that remain steady, so that the particle's charge gradually varies from zero toward its equilibrium value; in this case the charging time has been defined as the time required for a particle's charge to reach a fraction $(1 - e^{-1})$ of its equilibrium value. The charging time varies inversely with plasma density and particle size, according to [21]

$$\tau = K_{\tau} \frac{\sqrt{k T_{\mathrm{e}}}}{a n_{\mathrm{i}}} \quad , \tag{6.10}$$

where for a non-drifting plasma K_{τ} is a function of $T_{\mathrm{i}}/T_{\mathrm{e}}$ and $m_{\mathrm{e}}/m_{\mathrm{e}}$. The fact that τ is inversely proportional to both a and n_{i} means that the fastest charging occurs for large particles and high plasma densities. Values of the constant K_{τ} are summarized in table 6.1.

Table 6.1: Coefficients for $\phi_{\rm f}$, Q and τ appearing in Equations (6.8), (6.9) and (6.10). These values were found by a numerical solution of the continuous charging model, assuming non-drifting Maxwellians and no electron emission.

m_i (amu)	$T_{\rm e}/T_{\rm i}$	K_ϕ (V/eV)	$K_{\rm Q}(\mu{\rm m}^{-1}\,{\rm eV}^{-1})$	$K_\tau(\sec\mu{\rm m}\,{\rm cm}^{-3}\,{\rm eV}^{-1/2})$
1	20	-1.698	-1179	766
1	1	-2.501	-1737	1510
40	20	-2.989	-2073	2050
40	1	-3.991	-2771	3290

No dust particle is perfectly spherical, and so one should ask how much the spherical assumption limits the theory's validity. This assumption appears twice in the model: the capacitance in equation (6.2) and the currents in equation (6.4). For a dielectric particle, Eq. (6.2) is inappropriate for a non-spherical particle, as described above. For a conducting particle, on the other hand, capacitance is a meaningful concept, and the value of the capacitance does not depend extremely sensitively on the particle shape provided one chooses for a the typical size of the particle. The electron and ion currents are dominated by the shape of the electrostatic equipotential surfaces around the particle. The electric perturbation caused by the particle extends into the plasma a distance characterized by the shielding length, $\lambda_{\rm D}$. Since the case treated here is $a \ll \lambda_{\rm D}$, the equipotentials are distorted from a spherical shape only in a small central part of a spherical region of radius $\lambda_{\rm D}$. Consequently, the spherical assumption will introduce only a small error, as long as $a \ll \lambda_{\rm D}$, as it is in most dusty plasmas.

6.2.2 Reduction of the charge due to high particle density

So far, we have considered the case of a single isolated particle, but this assumption is often unsuitable for modeling dusty laboratory plasmas, since they can have high particle concentrations. As the dust number density is increased, the particle's floating potential and charge are reduced, due to electron depletion on the particles [1]. This electron depletion also modifies the plasma potential. The crucial parameter is Havnes' value P, which is basically the ratio of the charge density of the particles to that of the ions. When $P > 1$, the charge and floating potential are significantly diminished, while for $P \ll 1$ the charge and floating potentials approach the values for an isolated particle. In practical units [22],

$$P = 695\, T_{\rm eV} a_{\mu{\rm m}} \frac{n_{{\rm d},{\rm cm}^{-3}}}{n_{{\rm i},{\rm cm}^{-3}}}\,, \tag{6.11}$$

where $n_{\rm d}$ and $n_{\rm i}$ are the dust and ion number densities, respectively, and the various parameters are in the units indicated by the subscripts. This expression is written in a form for a mono-dispersive size distribution; a more general expression for P accounting for size dispersion is offered by Havnes et al. [22].

To find the dust potential $\phi_{\rm s}$ for a given value of P, one should solve a set of equations:

$$\sum_{\alpha} I_{\alpha} = 0 \tag{6.12}$$

$$e(n_{\rm i} - n_{\rm e}) + n_{\rm d} C \phi_{\rm s} = 0 \quad . \tag{6.13}$$

In this set of equations, one should use expressions for the ion current based on equations (6.3), (6.4) or (6.5), depending on whether the ions are drifting. These expressions must also be adjusted for the electric potential of the plasma, as compared to the potential of a dust-free plasma.

Havnes [22] has reported graphs of the particle potential $\phi_{\rm s}$, as compared to the local plasma potential, as a function of P for hydrogen. As is typical for astronomical problems, for the ion density he assumed a Boltzmann response for ions, $T_{\rm e}/T_{\rm i} = 1$, and no ion drift.

Here, we present numerical solutions for particle potential $\phi_{\rm s}$ as a function of P for conditions more typical of laboratory dusty plasmas made by a gas-discharge plasma: the ion mass is 40 amu (argon), and $T_{\rm e}/T_{\rm i} = 80$. The equations we solved were (6.12) and (6.13), and for the ion current we used the most general expression, Eq. (6.4), along with Eq. 4.4 of Ref. [16]. We treated three cases: non drifting ions, ions drifting at $u_{\rm i}/C_{\rm s} = 0.1$ (somewhat slower than the ion thermal velocity as is typical in the main region of a glow discharge) and at $u_{\rm i}/C_{\rm s} = 1.0$ (as is typical near the sheath edge of a plasma that is bounded by an electrode). Here, $C_{\rm s} = kT_{\rm e}/m_{\rm i}$. For the ion density, in addition to the Boltzmann response that is traditional for astrophysical problems, we also treated the case of ions with a fixed density that did not vary in response to the local electric potential. We did this because the Boltzmann response is typically not an accurate model for ions in a gas discharge plasma, where the ions often have a dispersion of velocities that is small compared to the overall drift velocity.

Results are shown in figure 6.1. For ions that are streaming at high speeds in a sheath, the Boltzmann response (a) is an inappropriate assumption, and in that case the fixed-density approximation for ions (b) is more suitable.

In an rf discharge, the dust density is often high enough to attain $P \gg 1$. Consider for example the dust density measurements of Boufendi et al. [23]. In a silane rf discharge, particles grew to a radius $a = 115$ nm, as determined by electron microscopy. Mie scattering indicated a particle density of $n_{\rm d} = 1 \cdot 10^8$ cm^{-3}, while the ion density was $n_{\rm i} = 5 \cdot 10^9$ cm^{-3}, based on ion saturation current measurements using a Langmuir probe. Assuming $T_{\rm e} = 2$ eV, which is probably accurate to a factor of three, we estimate $P = 3.2$ (accurate to the same factor of three), corresponding to a 45 % reduction in the particle's charge (according to Eq. (6.11) and Fig. 6.1a).

6.2.3 Electron emission

Electrons can be emitted by the particle due to electron impact, UV exposure, thermionic emission, and field emission. The first two are probably the most important for laboratory dusty plasmas. Electron emission constitutes a positive current to the particle, and if it is large enough, it can cause the particle's charge to be positive, instead of negative as it is in the absence of electron emission. Even if the particle is not always positive, it might sometimes fluctuate to a positive level, as described below.

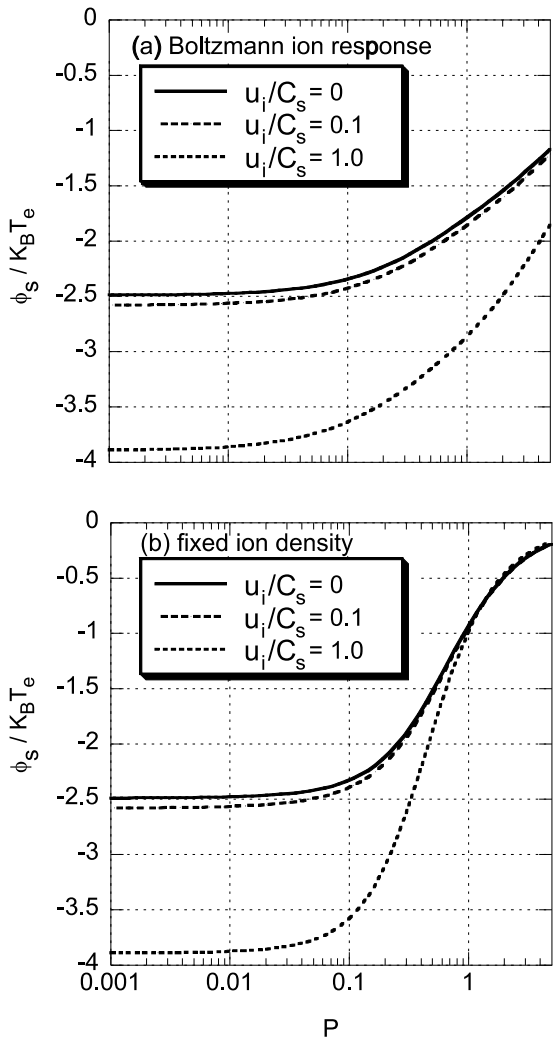

Figure 6.1: Electric potential of a dust grain, computed by solving Eq. (6.12) and (6.13) using the OML ion current, Eq. (6.4) and Eq. (4.4) of Ref. [16]. Results are shown as a function of the dimensionless dust density P, defined in (6.11). Data shown are for argon ions drifting at a speed $u_\mathrm{i}/C_\mathrm{s}$, and $T_\mathrm{e}/T_\mathrm{i} = 80$. In (a), the ion density varied exponentially with the local plasma potential according to the Boltzmann response, whereas in (b) the ion density was held constant regardless of the local plasma potential. The potential of an isolated dust grain corresponds to the solution at $P = 0$, which is $\phi_\mathrm{s}/kT_\mathrm{e} = -2.49, -2.58$, or -3.89; for $u_\mathrm{i}/C_\mathrm{s} = 0, 0.1$, or 1.0, respectively.

6.2.3.1 Secondary electron emission

The secondary emission yield δ depends on both the impact energy E and the particle material. The yield is generally much larger for electron impact than for ion impact. For bulk materials,

the energy dependence of the electron-impact yield is [24, 1]

$$\delta(E) = 7.4\delta_{\mathrm{m}} \frac{E}{E_{\mathrm{m}}} \exp\left(-2\sqrt{\frac{E}{E_{\mathrm{m}}}}\right) \quad . \tag{6.14}$$

The peak yield δ_{m} is at energy E_{m}, and both of these are material constants. Graphite, for example, has $\delta_{\mathrm{m}} = 1$ and $E_{\mathrm{m}} = 250$ eV, while for quartz $\delta_{\mathrm{m}} = 2.1 - 4$ and $E_{\mathrm{m}} = 400$ eV [24].

Secondary emission from small particles is significantly enhanced above the value for bulk materials. This was shown by Chow et al., [25] whose theory included geometric effects. Scattered electrons escape more easily from a small particle than from a semi-infinite slab of material, and so δ is enhanced.

Equation (6.14) is for mono-energetic electrons of energy E. It must be remembered that electrons in plasma have a distribution function. Assuming a Maxwellian primary electron distribution with temperature T_{e}, Meyer-Vernet [24] reported useful expressions for the secondary currents. By including these currents into the charging balance, the particle potential can become positive [24, 1]. For Maxwellian electrons, a reversal in polarity occurs at an electron temperature of 1 to 10 eV, depending on δ_{m}. The contribution of electrons in the tail of the distribution reason allows the reversal in polarity to occur at temperatures well below the energy for peak emission E_{m}.

6.2.3.2 Photoelectric emission

Absorption of UV radiation releases photoelectrons and hence causes a positive charging current. Just like secondary electron emission, it can make the particle positively charged [1].

The electron emission depends on the material properties of the particle (its photoemission efficiency). It also depends on the particle's surface potential, because a positively charged particle can recapture a fraction of its photoelectrons. Taking this into account, the photoemission current is [1]

$$I_\nu = 4\pi a^2 \Gamma_\nu \mu \qquad \phi_{\mathrm{s}} \leq 0 \tag{6.15}$$

$$I_\nu = 4\pi a^2 \Gamma_\nu \mu \exp\left(-e\phi_{\mathrm{s}}/kT_{\mathrm{p}}\right) \qquad \phi_{\mathrm{s}} \leq 0 \tag{6.16}$$

Here Γ_ν is the UV flux and μ is the photoemission efficiency ($\mu \approx 1$ for metals and $\mu \approx 0.1$ for dielectrics). Equation (6.15) assumes an isotropic source of UV and that the photoelectrons have a Maxwellian energy spectrum with a temperature T_{p}.

6.2.4 Ion trapping

A particle's negative charge creates a Debye sheath, which is an attractive potential well for positive ions. A passing ion can become trapped in this well when it suffers a collision within the particle's Debye sphere, simultaneously losing energy and changing its orbital angular momentum. It remains trapped there, in an orbit bound to the particle, until it is de-trapped by another collision [26].

Trapped ions can be important because they shield the charged particle from external electric fields. For example, if a dust particle with a negative charge $Q_{\rm d}$ is surrounded by $N_{\rm t}$ trapped positive ions, the dust particle will experience a diminished electric force, as if its charge were only $Q_{\rm d} + N_{\rm t}e$. This shielding works the same way as in an atom, where orbital electrons screen the charge of the nucleus.

Untrapped ions, unlike trapped ions, do nothing to screen the particle's charge from an electric field. Untrapped ions do, however, contribute to reducing the force applied by the particle on other distant charges. But they do not reduce the force applied to the particle by an electric field; only trapped ions can do that.

Ion trapping has been ignored often in dusty plasma theories, probably because it is not easy to model. At least two numerical methods [26, 27] have been reported, as well as an analytic model [28].

6.2.5 Charge fluctuations

The standard continuous charging model described in section 6.2 neglects the fact that the electron and ion currents collected by the particle actually consist of individual electrons and ions. The charge on the particle is an integer multiple of the electron charge, $Q_{\rm d} = Ne$, where N changes by -1 when an electron is collected and by $z_{\rm i}$ when an ion is absorbed. Electrons and ions arrive at the particle's surface at random times, like shot noise. The charge on a particle will fluctuate in discrete steps (and at random times) about the steady-state value $\langle Q_{\rm d}\rangle$.

Several models have been reported to predict the fluctuation level [27, 21]. One can think of the OML model as predicting a current that is actually a probability per unit time of collecting an electron or ion from the plasma. In this way, one can simulate the collection of discrete electrons and ions at random intervals, based on a meaningful probability, in a Monte Carlo code [21].

The fractional fluctuation is strongest for smallest particles. Cui and Goree [21] found that it obeys $Q_{\rm d}/\langle Q_{\rm d}\rangle = 0.5\langle Q_{\rm d}/e\rangle^{-1/2}$, for a wide range of plasma and particle parameters. The square-root scaling is the same as in counting statistics, where the fractional uncertainty of a count N is $N^{-1/2}$. The power spectrum of the fluctuations is dominated by very low frequencies, with half the spectral power lying at frequencies below $0.024\tau^{-1}$. Here τ is the charging time, as defined in Eq. (6.10). At higher frequencies, the spectral power diminishes as the second power of frequency, f^{-2}.

6.3 Forces on Particles

The main forces on dust particles in a plasma, namely electric field force, gravity, ion drag force, thermophoresis and neutral drag, are mostly irrelevant in usual plasmas and will therefore be briefly discussed, here.

6.3.1 Electric Field Force

The governing force on charged particles is the force in the electric field $\vec{E}$ given by

$$\vec{F}_{\mathrm{E}} = Q_{\mathrm{d}}\vec{E} = 4\pi\epsilon_0 a\phi_{\mathrm{fl}}\vec{E} \quad . \tag{6.17}$$

The force scales linearly with the particle size as predicted by the capacitor model in Sec. 6.2.1. Hamaguchi and Farouki [29] have discussed the question of whether a shielding cloud around the dust particle would lead to a modification of the electric field force. They found that modifications to the electric field force would only have to be considered when the shielding cloud is distorted. In that case, polarization forces on the particles might exist which can be written as

$$\vec{F}_{\mathrm{dip}} = \vec{\nabla}(\vec{p}\cdot\vec{E})$$

where $\vec{p}$ the dipole moment. Dipole moments can either be induced by an external electric field [30] or by directed charging processes (for dielectric particles) where due to an ion flow the front side of the particle is charged more positively than the back side [31]. Polarization forces are usually considered negligible, except for very large particles [32].

6.3.2 Gravity

The gravitational force simply is

$$\vec{F}_{\mathrm{g}} = m_{\mathrm{d}}\vec{g} = \frac{4}{3}\pi a^3\rho_{\mathrm{d}}\vec{g} \quad . \tag{6.18}$$

with the gravitational acceleration $\vec{g}$ and the mass density of the dust particles ρ_{d}. This force obviously scales as a^3. Thus, it is a dominant force for particles in the micrometer range and becomes negligible for nanometer particles.

6.3.3 Ion Drag Force

Ions streaming past a dust particle exert a force on the dust by scattering of the ions in the electric field of the dust or by collection on the dust surface. In a plasma discharge there always is a persistent ion stream either due to ambipolar diffusion in the plasma bulk or due to the electric fields in the plasma sheath. The ion drag force is one of the major forces on dust particles. It is understood qualitatively, but a complete quantitative description is still missing due to the complexity of the involved processes.

The ion drag consists of two parts, the collection force $\vec{F}_{\mathrm{coll}}$ due to ions hitting the dust and the Coulomb force $\vec{F}_{\mathrm{Coul}}$ due to scattering of the ions in the electrostatic field of the dust [33, 34, 35, 36, 37]. The total ion drag force is then given by

$$\vec{F}_{\mathrm{ion}} = \vec{F}_{\mathrm{coll}} + \vec{F}_{\mathrm{Coul}} \quad . \tag{6.19}$$

The ions which arrive at the particle not only contribute to ion charging of the dust, but also transfer their momentum to the dust and thus exert the collection force on the dust. This

force is given by [34]

$$\vec{F}_{\mathrm{coll}} = m_{\mathrm{i}} v_{\mathrm{s}} n_{\mathrm{i}} \vec{u}_{\mathrm{i}} \pi a^2 \left(1 - \frac{2e\phi_{\mathrm{fl}}}{m_{\mathrm{i}} v_{\mathrm{s}}^2}\right) \quad . \tag{6.20}$$

Here, $v_{\mathrm{s}} = (u_{\mathrm{i}}^2 + v_{\mathrm{th,i}}^2)^{1/2}$ is the geometric mean of the ion drift velocity u_{i} and the ion thermal velocity $v_{\mathrm{th,i}}$. Upon impact, the ions transfer the momentum $m_{\mathrm{i}} u_{\mathrm{i}}$. Further,

$$\sigma_{\mathrm{coll}} = \pi b_{\mathrm{c}}^2 = \pi a^2 \left(1 - \frac{2e\phi_{\mathrm{fl}}}{m_{\mathrm{i}} v_{\mathrm{s}}^2}\right)$$

is the collection cross section and b_{c} is the maximum impact parameter for ion collection (This is related to the charging model in Sec. 6.2.1). Then, $n_{\mathrm{i}} \vec{v}_{\mathrm{s}} \sigma$ is the number of ions hitting the dust surface per unit time.

The Coulomb force is due to those ions which are deflected in the local electric field in the sheath surrounding the dust grain. It is given in an early formulation by Barnes et al. [34] as

$$\vec{F}_{\mathrm{Coul}} = m_{\mathrm{i}} v_{\mathrm{s}} n_{\mathrm{i}} \vec{u}_{\mathrm{i}} 4\pi b_{\pi/2}^2 \ln \left(\frac{\lambda_{\mathrm{D}}^2 + b_{\pi/2}^2}{b_{\mathrm{c}}^2 + b_{\pi/2}^2}\right)^{1/2} \quad , \tag{6.21}$$

where $b_{\pi/2} = Q_{\mathrm{d}} e/(4\pi\epsilon_0 m_{\mathrm{i}} v_{\mathrm{s}}^2)$ is the impact parameter for $90°$ scattering and

$$\sigma_{\mathrm{Coul}} = 4\pi b_{\pi/2}^2 \ln \left(\frac{\lambda_{\mathrm{D}}^2 + b_{\pi/2}^2}{b_{\mathrm{c}}^2 + b_{\pi/2}^2}\right)^{1/2}$$

is the cross section for Coulomb scattering [38]. In this formulation, only ion scattering in the Debye sphere of radius λ_{D} is considered. Perrin et al. [36] and Khrapak et al. [39, 40] have shown that due to the high charge on the dust, ion scattering outside the Debye sphere will decisively increase the strength of the ion drag force.

Ion-neutral collisions can substantially influence the ion drag. Recent simulations [41] have indicated that ion-neutral collisions can even lead to a force opposite to the ion motion. A kinetic approach including ion collisions [42] showed a modification to the ion drag force, but not a reversal of the ion drag force. Generally speaking, the experiments are in a range that is not fully covered by theoretical calculations that have been developed so far.

Experimentally, the ion drag force has been measured by dropping particles through an RF plasma (see Fig. 6.2). There the particles experience oppositely directed electric force and ion drag. Depending on the plasma power, the relative strength of the two forces can be varied [43]. From that experiment, good agreement was obtained with the Barnes formulation of the ion drag force. In a similar experiment the ion drag force was measured in a DC discharge [44]; the force has been explained with reasonable accuracy by the Khrapak model [40] that includes ion scattering outside the Debye sphere.

6.3.4 Thermophoresis

The thermophoretic force appears due to a temperature gradient in the neutral gas. In a simplified picture, neutral gas atoms from the “hotter” side that hit the dust grain transfer a larger

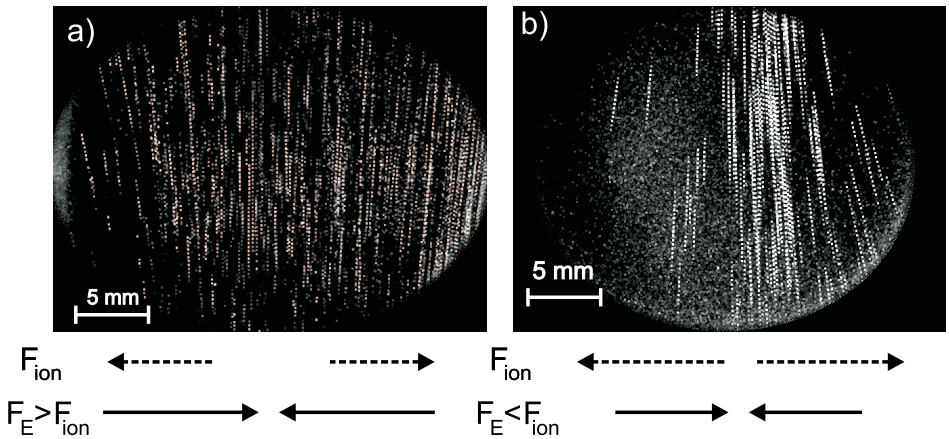

Figure 6.2: Particles of 4.8 μm diameter dropping through a cylindrical plasma discharge operated at a power of 2 W(a) and 5 W(b). At lower power the electric field force F_E exceeds the ion drag F_{ion} and the particles are focused to the center of the discharge. At higher power the particles are pushed away from the center due to the dominance of the ion drag. After [43].

momentum to the dust than atoms from the "colder" side. Consequently, a force towards regions of colder gas is established. From gas kinetic theory this force is [45, 46]

$$\vec{F}_{\mathrm{th}} = -\frac{32}{15}\frac{a^2 k_{\mathrm{n}}}{v_{\mathrm{th,n}}}\vec{\nabla}T_{\mathrm{n}} \tag{6.22}$$

where ∇T_{n} is the temperature gradient in the neutral gas and k_{n} the thermal conductivity of the gas. This formula holds if the mean free path of the gas molecules λ_{mfp} is much larger than the particle radius. The action of the thermophoretic force has been demonstrated by Jellum et al. [46]. In his experiments particles were driven towards cooled electrodes by thermophoresis or have even been removed from the discharge since the particles are collected at a liquid nitrogen cold finger placed near the plasma. Using heated electrodes the thermophoretic force has also been exploited to levitate particles (see below) [47, 48].

6.3.5 Neutral Drag Force

The neutral drag is the resistance experienced by a particle moving through a gas. For particles much smaller than the mean free path $a \ll \lambda_{\mathrm{mfp}}$ and particle velocities much smaller than the thermal velocity of the gas ($v_{\mathrm{d}} \ll v_{th,n}$) Epstein's expression [49] is appropriate

$$\vec{F}_n = -\delta\frac{4}{3}\pi a^2 m_{\mathrm{n}} v_{\mathrm{th,n}} n_{\mathrm{n}} \vec{v}_{\mathrm{d}} \quad . \tag{6.23}$$

Here, $m_{\mathrm{n}}, n_{\mathrm{n}}$ and $v_{\mathrm{th,n}}$ are the mass, the density and the thermal velocity of the neutral gas atoms, respectively. The parameter δ depends on the microscopic mechanism of the collision between the gas atom and the particle surface. In Epstein's model, δ can have a value in

the range between 1.0 and 1.442, where $\delta = 1.0$ is for specular reflection of all impinging molecules and $\delta = 1.442$ for diffuse reflection with accommodation, i.e. for a perfect thermal nonconductor. Recent experiments [50] with laser-driven polymer microspheres yielded $\delta = 1.26 \pm 0.13$. In connection with equations of particle motion we will often use the drag force in the form

$$\vec{F}_{\mathrm{n}} = -m_{\mathrm{d}}\beta\vec{v}_{\mathrm{d}} \qquad \beta = \delta\frac{8}{\pi}\frac{p}{a\rho_{\mathrm{d}}v_{\mathrm{th,n}}} \quad . \tag{6.24}$$

Here, β is the friction coefficient and linearly depends on the gas pressure p. The friction coefficient is inversely proportional to the particle radius a which means that in relation to their mass smaller particles experience stronger damping than larger particles.

6.3.6 Radiation Pressure Forces

Radiation pressure is the momentum per unit area and unit time transferred from photons to a surface. If a beam of photons strikes the particle, some photons will be reflected and others will be transmitted or absorbed. All three processes contribute to the radiation pressure. In general for a laser beam of intensity I_{laser}, the radiation pressure force is [51]

$$F_{\mathrm{rad}} = \gamma\frac{\pi a^2 I_{\mathrm{laser}}}{c} \quad , \tag{6.25}$$

where c is the speed of light and γ is a dimensionless factor that is determined by the reflection, transmission or absorption of the photons on the particle. If all photons are absorbed γ will be 1, and for complete reflection $\gamma = 2$. Experimental investigations report this parameter to be $\gamma = 0.94 \pm 0.11$ for polymer microspheres [50].

Lasers are widely used in dusty plasmas to manipulate dust particles without disturbing the plasma environment. For example, they are used to measure forces or excite waves, Mach cones and resonances, see e.g. Fig. 6.19 and [52].

6.3.7 Particle Interaction Potentials

After the discussion of the plasma-related forces onto the dust particles we now will dwell on the interaction among dust particles.

6.3.7.1 Particles in Isotropic Plasmas

In isotropic plasmas, the particles are usually treated as point charges that are shielded by the ambient plasma background. Thus, the interaction is described by a Debye-Hückel or Yukawa potential energy

$$U(r) = \frac{Z_{\mathrm{d}}^2 e^2}{4\pi\epsilon_0 r}\exp\left(-\frac{r}{\lambda_{\mathrm{D}}}\right) \tag{6.26}$$

with the screening length λ_{D}. In a plasma with flowing ions, this model is known to be accurate only in the plane perpendicular to the ion flow. Experimentally, the interaction can

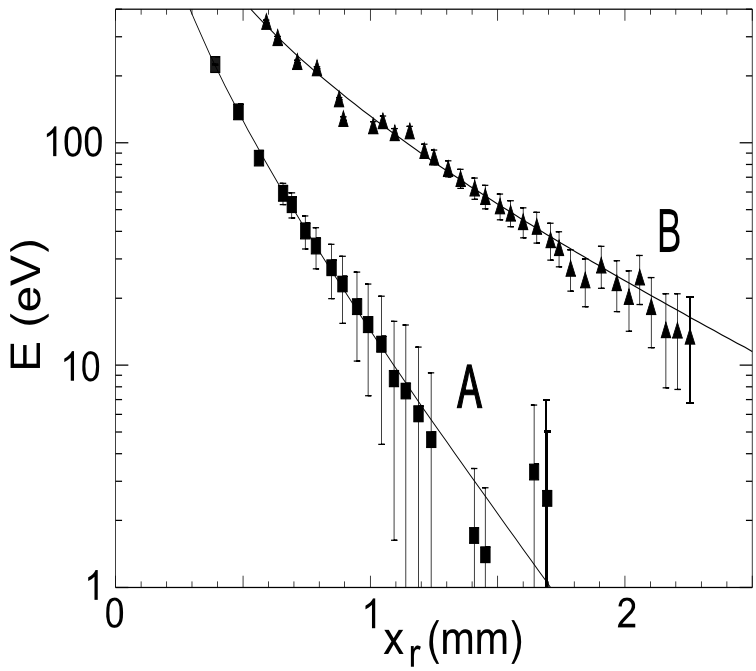

Figure 6.3: Measured horizontal interaction potential from collisions of two dust particles. The curves A and B reflect two different discharge conditions. From the experiment, $Z_\mathrm{d} = 13\,900$ and $\lambda_\mathrm{D} = 0.34$ mm (case A) and $Z_\mathrm{d} = 17\,100$ and $\lambda_\mathrm{D} = 0.78$ mm (case B) are deduced. After [53].

be precisely determined from the dispersion of waves, a method that will be presented in Sec. 6.6.2. Alternatively, the dust interaction has been probed by the analysis of collisions between dust particles [53]. There, two dust particles were forced to collide at different speeds and the collision dynamics has been analyzed. From the collisions the interaction has indeed been determined as a purely repulsive Yukawa potential with a screening length λ_D that is compatible with the electron Debye length λ_De, see Fig. 6.3.

6.3.7.2 Particles in the Plasma Sheath

Often, the dust particles are trapped in the plasma sheath where strong electric fields and a directed ion motion towards the electrode prevail. This strongly non-neutral, non-equilibrium environment drastically alters the particle-particle interaction. An obvious sign is the unexpected vertical alignment of dust particles in the sheath. There the particles are located directly on top of each other forming vertical chains [5, 54] which definitely is not a minimum energy configuration for purely repulsive particle interaction (see also Fig. 6.6).

Analytical models of the particle interaction in the plasma sheath have been put forward e.g. in [55, 56, 57, 31, 58, 30, 32, 59]. First detailed simulations and experiments of Schweigert et al. and Melzer et al. [60, 61, 62, 63] have revealed that the force between dust

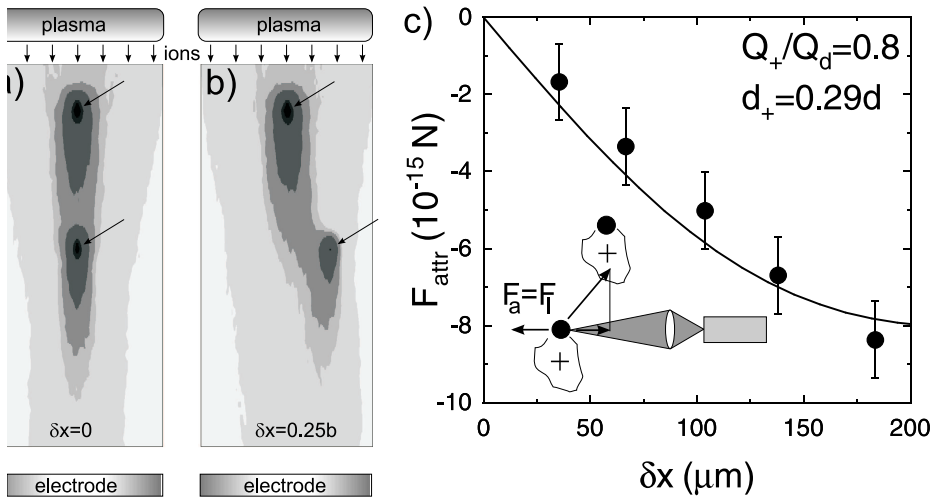

Figure 6.4: Simulated ion density distribution around dust particles in the plasma sheath when a) the dust particles are vertically aligned ($\delta x = 0$) and b) when they are shifted horizontally by a quarter of the interparticle distance ($\delta x = 0.25b$). c) Horizontal component of the attractive force on the lower particle as a function of displacement from the vertically aligned position. The symbols denote experimental values from laser manipulation and the solid line is derived from the simulations. The inset shows a sketch of the experimental setup of the force measurement. After [62, 61]

particles in the sheath is a very peculiar nonreciprocal, attractive force: dust particles located lower in the sheath are attracted by upper particles, but the upper particles experience a repulsive force from the lower.

The origin of this non-reciprocal attraction lies in the ion streaming motion in the sheath region between the plasma and an electrode (see Fig. 6.4a,b). The ions have entered the sheath with Bohm velocity and stream towards the electrode through the particle arrangement. The electric field of the upper dust particle deflects ions so that they are focused beneath the particle. This yields a region of enhanced positive space charge which provides the attraction for the lower particles. In other words, the shielding cloud around the dust particles is distorted downwards due to the ion streaming motion. This is often term a “wake effect”. Since the ions move at supersonic speed in the sheath the attractive force can only be communicated downwards and not upwards, which results in the peculiar situation that only the lower particle experiences attraction, but there is no reaction on the upper particle. The attraction by the ion cloud is stronger than the repulsion from the upper particle since the ion cloud is located closer to the lower dust particle.

The nonreciprocal attraction has been directly demonstrated using laser manipulation techniques [60, 61, 64] in a system with two vertically aligned particles. The lower particle was elongated from the vertical position by the radiation pressure of a laser beam. From the force balance of laser pressure and attractive force the attraction is determined (see Fig. 6.4c). The simulations and the experiments suggest that the distorted ion cloud beneath the dust particle can be modeled by a single positive point charge of charge Q_+ located at a position $d - d_+$

below the dust. From the experiment, $Q_+ = 0.8Q_\mathrm{d}$ and $d_+ = 0.29d$ are obtained in good agreement with the simulations [62].

6.4 Experimental Methods

Dusty plasmas enable to confine particles in custom-tailored configurations and geometries by exploiting the various forces on the dust. In this section, a few selected examples will be presented. In addition, techniques of the observation, identification, and diagnostics of the confined particle arrangements will be shown.

6.4.1 Particle Confinement and Levitation

In the laboratory, dust plasmas are usually confined in discharge plasmas, mainly in RF parallel plate discharges, but also DC discharges are frequently used. A selection of particle confinement schemes will be summarized here.

6.4.1.1 RF Discharges

Radio-frequency (RF) discharges between parallel electrodes are the main tool of dusty plasma research because RF discharges easily tolerate impurities and they are also used in plasma processing where dust-contamination occurs. RF discharges for dusty plasma research are typically operated at 13.56 MHz at relatively low RF powers (usually <10 W) and gas pressures in the range between 1 and 100 Pa.

The general setup for dust experiments in RF parallel plate discharges is shown in Fig. 6.5. A discharge is operated between the parallel electrodes, usually the lower is RF powered and the upper is grounded. Often, the upper electrode has openings or is transparent to have optical access from top. The dust particles are then dropped into the discharge using dust containers with tiny holes. Typical dust for basic research consists of spherical plastic particles of well-defined diameter in the micrometer range (see Fig. 6.5b).

For micrometer particles, the dominant forces are the electric field force and gravity. A force balance is achieved in the plasma sheath above the lower electrode where the electric field is strong enough to levitate the particles against their weight. Since the electric field is increasing towards the electrode the force balance is fulfilled at a unique vertical position and the particles are confined in a an effective vertical potential well (Fig. 6.5c). With the large electrodes that can be used in RF discharges, horizontally extended plasma crystals with a small number of vertical layers are produced. Figure 6.6 shows monolayer and two-layer crystals of large horizontal extent. Note the vertically aligned particle positions in the two-layer crystal due to the non-reciprocal attraction in the plasma sheath.

With barriers on the electrode, the confinement for the dust particles can easily be modified leading to different dust configurations, see Fig. 6.7. Linear (1D) particle chains can be achieved by a groove in the electrode [50, 67, 68], and two-dimensional (2D) clusters are generated with an electrode having a parabolic trough [69, 70]. With these barriers the equipotential lines in the plasma sheath are distorted, thus yielding an additional horizontal component of the electric field force that leads to a confinement also in the horizontal plane.

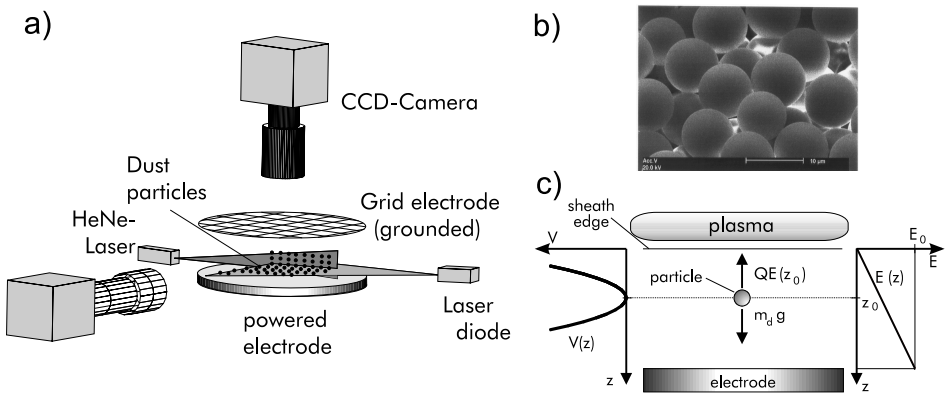

Figure 6.5: a) Scheme of the experimental setup in a typical experiment on complex plasmas. The particles are illuminated by vertical and horizontal laser sheets. The particle motion is recorded from top and from the side with video cameras. b) Electron micrograph of the melamine-formaldehyde (MF) particles typically used in the experiments. c) Trapping of the particles in the sheath of an rf discharge. See text for details.

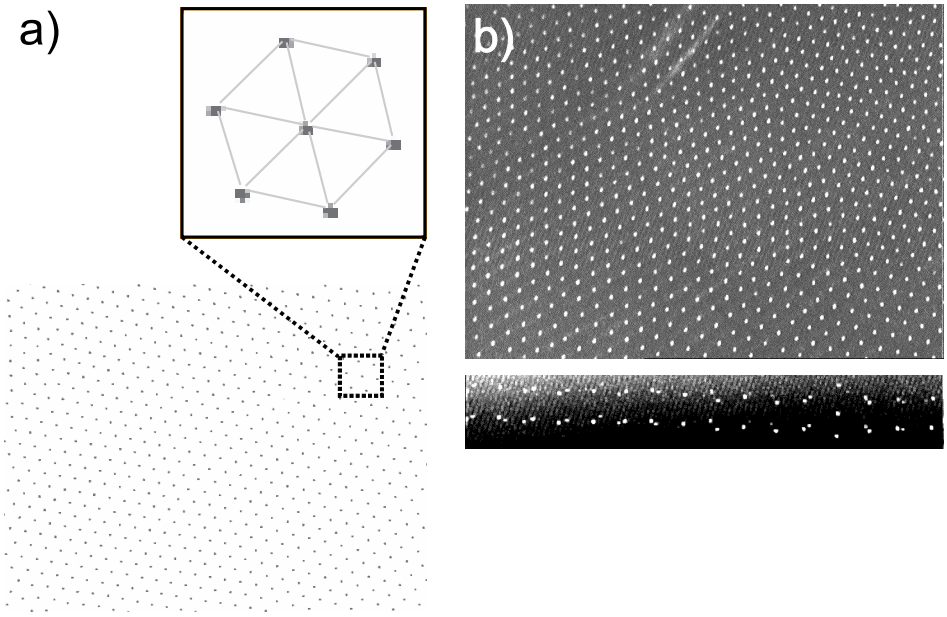

Figure 6.6: a) Monolayer crystal with hexagonal symmetry (see insert) and b) two-layer plasma crystal (top and side view). In the two-layer crystal the horizontal plane also has hexagonal symmetry, but the particles of the two layers are positioned directly above each other reflecting the non-reciprocal attraction in the sheath. After [65, 66].

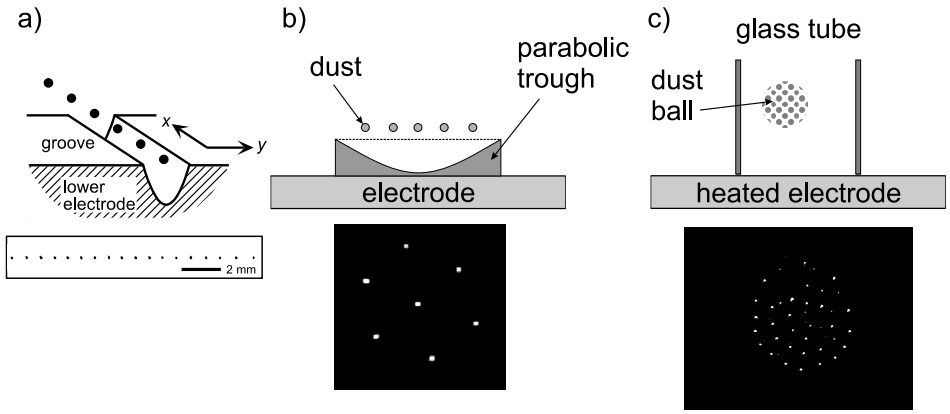

Figure 6.7: Particles in RF discharges with tailored confinement forming a) linear arrangements (1D clusters, here with $N = 18$ particles, after [68]), b) two-dimensional (2D) clusters (here with $N = 7$ particles, after [69]) and c) three-dimensional dust balls (3D clusters, here a cross section through a cluster with $N = 190$ particles, after [48]).

Recently, even highly ordered full 3D arrangements have been produced [48]. There, gravity was (at least partially) compensated by thermophoretic forces due to a heated electrode. The horizontal confinement was due to dielectric glass walls. In this confinement, nearly spherical dust clouds can be trapped.

With these techniques charged particle systems under various confinement geometries have been studied and the influence of geometry and confinement on the structure and dynamics are investigated.

6.4.1.2 DC Discharges

Dusty plasmas are also studied in a vast number of DC discharges ranging from glow discharges via thermionic discharges to Q-machines.

Glow discharges in glass tubes are usually operated between 10 and 500 Pa at discharge currents between 0.1 to 10 mA [12]. In vertically arranged tubes the particles are usually trapped in the standing striations that appear under certain conditions in the positive column of the discharge. There the electric field that goes along with the striations is strong enough to levitate the particles against gravity. The particles arrange in cylindrical or spherical clouds that often show high wave activity [71].

Often dust particles are trapped in the anode spot of glow discharge or Q-machine plasmas [72, 73, 74]. There, spherical or cylindrical dust clouds are trapped against gravity in the electrostatic potential near the anode. Also these clouds usually show strong particle fluctuations and wave activity which are probably driven by the current to the anode.

A distinction of DC plasmas, as compared to RF plasmas, is that the instantaneous and time-averaged electric fields are the same. Consequently dust and electrons behave similarly in DC plasmas, despite their tremendously different masses. In RF plasmas, on the other hand, electrons can respond to megahertz frequency reversals of the electric field, whereas the

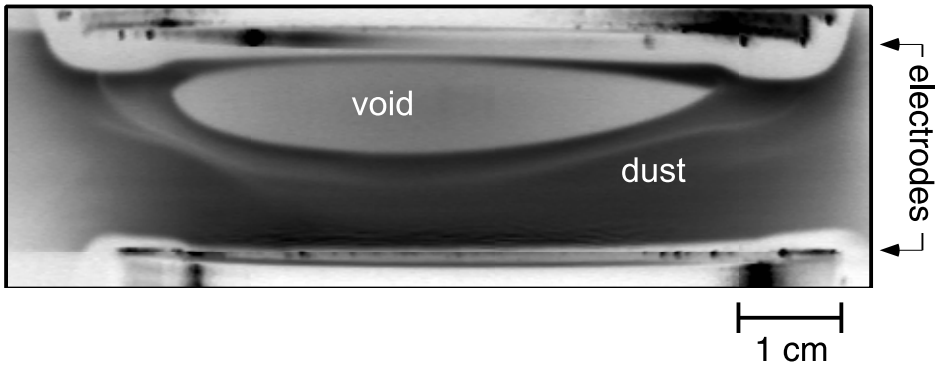

Figure 6.8: In plasmas that contain dust particles in the plasma volume, usually a void is formed. The void is a region usually in the central part of the discharge from which the particles are expelled. This is seen here in a discharge that contain nanometric carbon particles appearing as a dark cloud. In contrast, the void region is free of dust. After [76].

heavier dust particles cannot. Thus, electrons can easily move into spatial regions where dust cannot. This difference between DC and RF plasmas has a significant effect on the ability to levitate dust particles. In an DC plasma, the most of the sheath has an insignificant electron density and therefore if a dust particle finds itself immersed deep inside a DC sheath it will collect only ions and become charged positively, which results in a force directed toward the electrode rather than away so that a horizontal electrode is unable to levitate dust particles located deep in the sheath above it. In an RF plasma, the sheath collapses and expands at the applied radio frequency so that the time-averaged electron density is everywhere non-zero in the sheath. Thus, a dust particle can collect electrons and maintain a negative charge no matter where it might be located inside the sheath. Thus for an RF discharge a particle can be levitated either deep in a sheath where the electric field is largest or near the edge of the sheath where it is weakest, but in a DC discharge a particle can be levitated only near the edge of the sheath.

6.4.1.3 Discharges with Nanoparticles

For particles in the nanometer range gravity is not important, thus smaller electric fields are sufficient to levitate and trap the particles. The electric field force is inwards to the plasma bulk for negatively charged particles. Usually, ion drag and thermophoresis usually point outward. Thus, trapping of dust particles should be possible in the entire plasma volume and three-dimensionally extended dust clouds are expected. However, in plasmas with nanometer particles large dust-free regions occur from which the dust is expelled [75, 76], see Fig. 6.8. These so-called “voids” have well-defined boundaries which are assumed to be due to the force balance of the ion drag and electric field force [77, 78]. Voids are a general phenomenon and can hardly be avoided. For example, they also appear in experiments under microgravity where gravity is obviously irrelevant.

6.4.2 Charge Measurement Methods

The governing parameter in dusty plasmas is the charge on the dust particles as described in Sec. 6.2. Experimentally, the dust charge of particles in the plasma sheath has been determined from the resonance method which is briefly described, here [79, 54].

6.4.2.1 The potential well

As shown above, in typical laboratory rf discharges the particles are trapped by a force balance of gravity and electric field force

$$Q_0 E(z_0) = m_\mathrm{d} g \quad . \tag{6.27}$$

Considering the spatially dependent electric field $E(z)$ in the sheath the particles are trapped at the unique equilibrium position z_0. The equation of motion for vertical oscillations around z_0 is then given by

$$\ddot{z} + \beta \dot{z} + \frac{Q_0 E(z)}{m_\mathrm{d}} = F_\mathrm{ext} \quad , \tag{6.28}$$

where β is the friction coefficient describing the neutral gas drag (see Eq. 6.24) and F_ext are other external forces applied to the particle.

For small deviations from the equilibrium position the electric field can be assumed linearly increasing $E(z) = E(z_0) + E'(z - z_0)$ with $E' = \partial E/\partial z =$ const. Under these assumptions the microspheres are trapped in a harmonic potential well [79, 54]

$$\frac{1}{2} m_\mathrm{d} \omega_\mathrm{res}^2 (z - z_0)^2 = \frac{1}{2} Q_0 E' (z - z_0)^2 \tag{6.29}$$

with a resonance frequency of

$$\omega_\mathrm{res}^2 = \frac{Q_0}{m_\mathrm{d}} E' \quad . \tag{6.30}$$

The resulting resonance curve is that of a damped harmonic oscillator. Thus, the measurement of the vertical resonance of a trapped particle allows to determine the charge-to-mass ratio and the particle charge Q_0 [79, 54].

The linearly increasing electric field (with the slope E') is determined from the assumption of a constant space charge density (the so-called ion matrix sheath) $e(n_\mathrm{i} - n_\mathrm{e}) = \epsilon_0 E'$. The linear electric field model is supported by a number of simulations of rf discharges [80, 81, 82] and theoretical analysis [83]. This allows the connection of the sheath electric field to the ion density measured by Langmuir probes in the bulk plasma.

6.4.2.2 Linear Resonances

The charge measurements have been performed using monodisperse melamine-formaldehyde (MF) microspheres (see Fig. 6.5b). Vertical oscillations in the potential well were driven by applying a very low-frequent modulation of the electrode rf voltage, see Fig. 6.9a. In doing so,

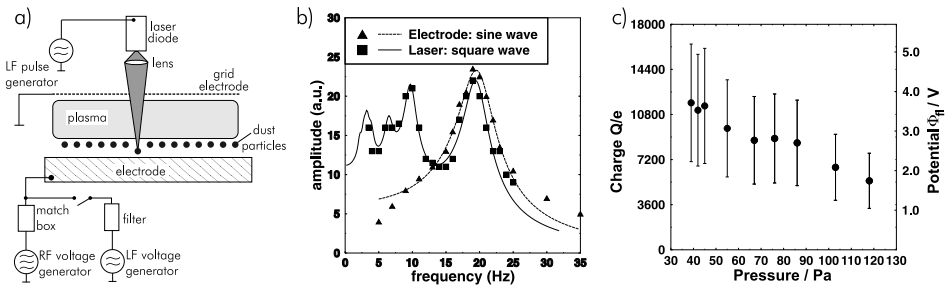

Figure 6.9: Measuring the charge on MF microspheres. a) Experimental setup for excitation of resonances by rf voltage modulation and laser manipulation. b) Resonance curves obtained for a $9.47\ \mu$m MF particle for both excitation techniques. c) Measured dust charge as a function of discharge pressure. The uncertainty in the measured values of due to the uncertainty of the ion matrix sheath. From [66, 84].

the sheath width is modulated and the particle is forced to oscillate in the trapping potential well. The resonance curve was obtained by simply measuring the oscillation amplitude as a function of excitation frequency, see Fig. 6.9b, where a resonance is observed near 20 Hz. The particle charges calculated from (6.30) are found to be about 10 000 elementary charges and the floating potential is about 3 V (Fig. 6.9c) which is in reasonable agreement with estimations based on OML charging. The width of the measured vertical resonance peak is determined by the neutral gas drag on the particle and is in quantitative agreement with the Epstein [49] friction coefficient β in (6.28).

For comparison, the laser radiation force has been used to excite vertical resonances [84]. There, a laser beam is focused onto a single dust particle which is then pushed by the radiation pressure of the beam. By periodically switching "on" and "off" the laser beam vertical oscillations are driven. Comparing the main resonance frequency $\omega_{\rm res}$ measured from laser manipulation with that from the voltage modulation no difference within experimental errors is found. By laser excitation additional spurious resonances at $\omega_{\rm res}/2$, $\omega_{\rm res}/3$ etc. are excited due to the square wave laser excitation (laser "on" and "off").

A procedure very similar to the resonance technique is followed by Tomme et al. [85] who have studied damped oscillations of microspheres that have been dropped into the sheath. By using particles of different sizes a large part of the sheath has been explored. From this, the linear electric field profile and the charge values from the resonance technique have been confirmed.

6.4.2.3 Nonlinear Oscillations

Besides the linear resonances discussed above also nonlinear vertical oscillations have been observed [86, 87, 88].

Parametric resonances have been excited by a wire placed close to the dust particles in the sheath [86]. Applying a sinusoidal signal with low voltage to the wire a simple vertical resonance at ω_0 was observed as in the case of the electrode modulation. At higher voltages, however, a second resonance at $2\omega_0$ appeared (see Fig. 6.10a). The presence of the second

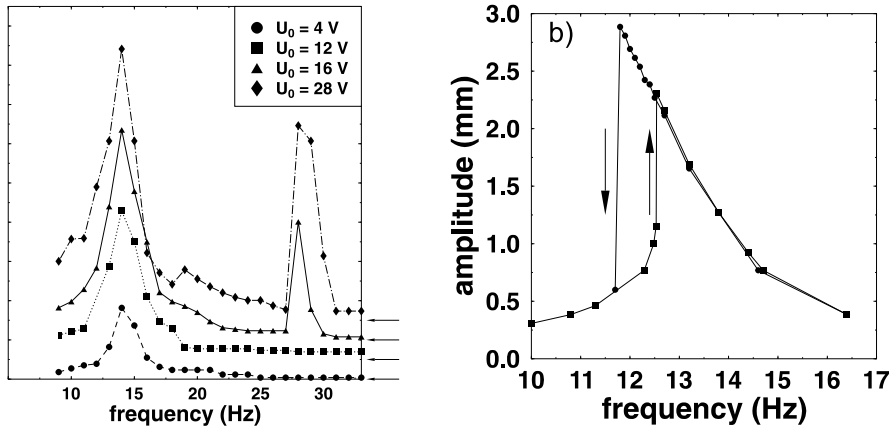

Figure 6.10: a) Parametric resonances observed at $2\omega_0$ for high excitation voltages on a wire close to the dust particles. From [86]. b) Nonlinear resonance for high voltages using the electrode modulation technique. From [88].

harmonic at $2\omega_0$ is an indication of parametric resonance. Parametric resonances are observed when the confining harmonic potential is periodically modulated. In this case, the electric potential on the wire in the sheath disturbs the potential well for the particles in the sheath leading to the observed parametric excitation.

A different type of nonlinearity has been observed in experiments of Ivlev et al. [87] and Zafiu et al. [88]. There a large amplitude sinusoidal voltage has been applied to a wire [87] or to the lower electrode [88]. Besides the observation of a second harmonic, the main resonance was found to exhibit hysteretic behavior accompanied by a strong asymmetry (see Fig. 6.10)b. This type of behavior can be explained when the confining potential becomes anharmonic at large particle oscillation amplitudes. From the analysis of the nonlinear resonance, Zafiu et al. [88] were able to relate the nonlinearity to a position dependent dust charge $Q(z)$. The spatial dependence of the dust charge is due to the reduction of electron density deep in the sheath and thus to a reduced electron charging of the particle.

The effect of a position dependent dust charge and finite charging times can lead to the onset of self-excited vertical oscillations [89]. Energy can be gained when during an oscillation the actual dust charge is different from the equilibrium charge at that point due to delayed charging. When that energy gain can compensate energy loss due to friction growing oscillations can be observed.

6.4.3 Particle Imaging and Tracking

Particles can be imaged using a video camera, as sketched in Fig 6.5. Most often, particles are illuminated by a sheet of laser light. The sheet can be generated for example by a diode laser fitted with a line generator, or a HeNe laser fitted with a cylindrical lens. Before passing through the cylindrical lens, the light is sometimes focused by a pair of spherical lenses, so that in the region viewed by the camera the laser sheet will have a desired thickness of typically

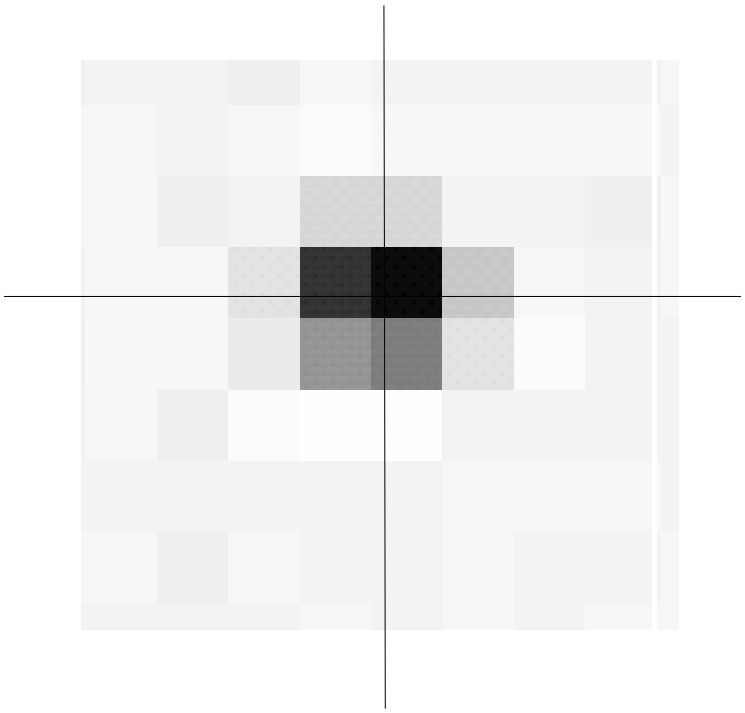

Figure 6.11: Part of a CCD video image containing a single dust particle. The particle appears as a ensemble of several dark pixels (The intensities are inverted, here). Using the moment method, the particle position can be determined with sub-pixel resolution. The reconstructed particle position is indicated by the solid lines.

0.1 mm. One can use the theory of Gaussian optics to predict the thickness of a focused laser beam.

The video camera can be either an analog camera (NTSC or PAL), or a digital camera. Analog cameras have the advantage of being low cost, and allowing inexpensive storage of videos. Images from analog cameras are digitized, to allow computer image analysis, by using a frame grabber or a digital VCR. Analog cameras have several disadvantages, including the fact that a video frame image is actually a interlaced superposition of two separate "field" images that were recorded at different times. Digital cameras do not have this limitation, and in many cases they allow higher frame rates or larger numbers of pixels than analog cameras. However, they consume greater resources, not only in the initial purchase, but also for data storage. In both cases, the hardware element for forming the image is a CCD chip.

The camera is typically used with a lens that provides a magnification of approximately 1:1 or less. At this magnification, a particle (typically < 10 micron diameter) fills less than one pixel on the CCD chip. Nevertheless, because of "blooming", several pixels will be illuminated, as shown in Fig. 6.11. This is actually a desirable feature, as it allows greater precision in determining the particle precision, as discussed below.

Using a bit-mapped image, as shown in Fig. 6.11, one can compute the particle's $x - y$ coordinates. If only one pixel were illuminated, then this would be done simply by assigning the particle to the center of that pixel. On the other hand, if several pixels are illuminated, the user has a choice of several methods for computing the particle position.

A computationally-efficient method of computing the particle's $x - y$ coordinate is the moment-method. In this method, the input data are the intensity I_i and center coordinates (X_i, Y_i) of each pixel i. One can subtract the background intensity $I_{\rm back}$ in the image, to improve the accuracy as discussed below. Then, in the moment method, one computes the particle position as

$$\begin{aligned} x &= \frac{\sum X_i (I_i - I_{\rm back})}{\sum (I_i - I_{\rm back})} \\ y &= \frac{\sum Y_i (I_i - I_{\rm back})}{\sum (I_i - I_{\rm back})} \quad . \end{aligned}$$

This yields a measurement, with sub-pixel resolution, as illustrated in Fig 6.11. As a practical matter, one must choose which pixels to include in the sums, and there are several algorithms for making this choice. One algorithm is to identify a particle as consisting of all contiguous pixels that are brighter than a threshold level chosen by the user.

A limitation in the accuracy of the moment method is that it tends to assign particles most often to special positions, most often the corners of a pixel, the center of a pixel, or the midpoint of a pixel's edge. This shortcoming is termed "pixel-locking", and it is most severe when only a few pixels are illuminated. In the most extreme case, when only one pixel is illuminated, a particle is assigned always to the center of a pixel and the accuracy of the method is $\pm 1 \mathrm{pixel}$. The larger the number of pixels that are illuminated, the smaller the pixel-locking effect and the better the sub-pixel resolution. For this reason, blooming of the CCD and defocusing of the lens can be desirable.

There are several methods available for attempting to reduce the effects of pixel-locking. One of the simplest is to reduce the threshold level when identifying particles. This threshold level, however, cannot be reduced arbitrarily small, because noise in pixels is finite, and could be mistakenly identified as particles if the threshold is set too small.

Once a particle's coordinates are established by a measurement method such as the moment method described above, a particle can be tracked from one frame to the next. This is done using a so-called "tracking" or "threading" algorithm. A simple and widely-used method is the following. First, establish the coordinates (x_j, y_j) in frame j using the moment method or a similar method. Next, in frame $j + 1$ search for a particle within a square box centered at the coordinates (x_j, y_j) where the particle was previously located. The size of this search box can be adjusted to minimize two undesired outcomes: zero particles are found in the search box, and more than one particle is found in the search box. For the successful outcome that only one particle is found in the search box in frame $j + 1$, this particle is assumed to be the same particle as in the previous frame. This method works well if particles remain in the illuminated laser sheet, and if the frame rate of the camera is sufficiently high.

The velocity of a particle is calculated simply as the difference in the position in two consecutive frames, $x_{j+1} - x_j$ multiplied by the frame rate. The user must keep in mind that due to pixel-locking, the most probable velocities will be integer or half-integer multiples of the pixel size per frame.

Repeating the tracking process until a particle is eventually lost from the image, one can create a long time series for particle positions, allowing a calculation of correlation functions for example.

6.5 Strongly Coupled Systems and Plasma Crystallization

As shown, the particles in dusty plasmas can form highly-ordered crystal-like structures. Here, we address the questions under which conditions plasma crystals are formed and what is their preferred structure.

6.5.1 Phase diagram of charged-particle systems

Charged-particle systems are described by the Coulomb coupling parameter which is defined as the ratio of the electrostatic energy of neighboring particles and their thermal energy,

$$\Gamma = \frac{Z^2 e^2}{4\pi\epsilon_0 b_{\mathrm{WS}} k T_{\mathrm{d}}} \quad , \tag{6.31}$$

where T_{d} is the dust temperature and $b_{\mathrm{WS}} = (3/4\pi n_{\mathrm{d}})^{1/3}$ is the Wigner-Seitz radius which is of the order of the interparticle distance b. A system is said to be strongly coupled when the electrostatic interaction exceeds the thermal energy, i.e. when $\Gamma > 1$.

The most simple case is a system of point charges with pure Coulomb interaction, the so-called one-component plasma (OCP). From simulations it is found [90] that crystallization of the charges occurs when Γ exceeds the critical value of $\Gamma_{\mathrm{c}} = 168 \pm 2$. A system with $1 < \Gamma < \Gamma_{\mathrm{c}}$ is in the liquid state, but still strongly coupled.

In a dusty plasma, the dust charge is shielded by the ambient plasma and the interaction is described by a Debye-Hückel or Yukawa energy (Eq. 6.26). Such a Yukawa system is characterized by a second parameter, the screening strength $\kappa = b_{\mathrm{WS}}/\lambda_{\mathrm{D}}$ which denotes the interparticle distance in units of the screening length. For $\kappa \to 0$ the OCP limit is retrieved. The phase diagram in the Γ–κ plane of a 3D Yukawa system, as found using numerical simulations, is shown in Fig. 6.12. The critical coupling parameter for the fluid-solid transition increases almost exponentially with the screening strength κ [91]. The phase diagram for a 2D Yukawa system was reported in [92].

For 3D particle arrangements with isotropic interactions, the preferred crystal structure is body-centered cubic (bcc) at low values of the screening strength. At higher κ a transition to face-centered cubic (fcc) takes place that has a higher packing density than bcc. In two dimensions, the hexagonal structure is the ground-state configuration where one particle is surrounded by 6 nearest neighbors forming a hexagon. In multi-layer systems, square lattices, bcc or hexagonal are expected [93].

Although also other crystal structures have been observed [94, 95], typically, in dusty plasma experiments hexagonal structures are found (see Fig. 6.6). The structures of multi-layer plasma crystals usually does not change between different lattice types. Rather, due to the strong vertically anisotropic interaction of particles in the plasma sheath, the crystals should be more considered as two-dimensional arrangements of vertical chains.

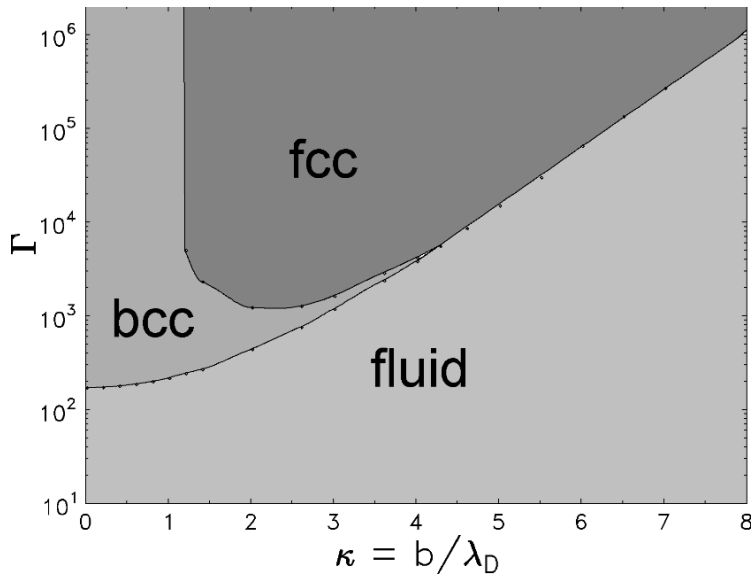

Figure 6.12: a) Phase diagram of the 3D Yukawa system. After [91].

6.5.2 Correlation Functions

Correlation functions allow to characterize and quantify particle arrangements. For laboratory dusty plasmas the analysis of two-dimensional systems is most relevant. Since the solid-liquid transition in 2D is believed to be continuous [96] the 2D correlations are very important in defining the state of the system.

One tool to analyze particle configurations is the pair correlation function $g(r)$, also known as the radial density function. This function represents the probability of finding two particles separated by a distance r and it measures the translational order in the structure. For large distances $r \to \infty$, the pair correlation function approaches unity $g(r) \to 1$ since one will always find a particle at a large distance r. Because the particles cannot come infinitely close to each other $g(r) \to 0$ for $r \to 0$.

Another tool is the bond-orientational correlation function $g_6(r)$ which is defined in terms of the nearest-neighbor bond angles θ of a lattice. It measures the orientational order in the structure, based on the principle that all bonds in a perfect hexagonal lattice should have the same angle, modulo $\pi/3$, with respect to an arbitrary axis. The angular correlation is defined as

$$g_6(r) = \langle \exp\left(6i\left[\theta(r) - \theta(0)\right]\right)\rangle \tag{6.32}$$

where the average is taken over the entire particle ensemble. For a perfect crystal at zero temperature, g_6 is a constant equal to unity while for other phases it decays with increasing r. Defects, i.e. particles that have 5 or 7 neighbors instead of the expected 6 in a hexagonal lattice, destroy the angular correlation g_6, but only weakly affect the pair correlation g.

In condensed matter physics, the pair correlation function for materials such as metals usually cannot be determined directly. Rather, the structure factor is determined from scattering of x-rays or neutrons. In dusty plasmas, we are able to measure the pair correlation function directly and then *calculate* the structure factor in order to compare with condensed matter experiments. The structure factor $S(q)$ is just the Fourier transform of the pair correlation function

$$S(\vec{q}) = 1 + n_{\mathrm{d}} \int (g(r) - 1) \exp(i\vec{q} \cdot \vec{r})\, d\vec{r} \quad , \tag{6.33}$$

where $\vec{q}$ is the wave vector of the scattered radiation. In 2D, this can be written as

$$S(q) = \frac{1}{N} \sum_{ij}^{N} \frac{1}{2\pi} \int_0^{2\pi} \exp(iqr_{ij} \cos\varphi)\, d\varphi = \frac{1}{N} \sum_{ij}^{N} J_0(qr_{ij}) \quad ,$$

where φ is the angle between $\vec{r}$ and $\vec{q}$ and J_0 is the zero-order Bessel function.

6.5.3 Phase Transitions

Phase transitions of plasma crystals from an ordered, solid state to a fluid and gas-like state have been observed experimentally [66, 97]. For instance, the melting transition is observed when the gas pressure in the discharge is reduced [66, 97]. At high gas pressures (118 Pa) well ordered crystalline structures are found (Fig. 6.13a). The particles do not move considerably, they stay in their respective Wigner-Seitz cells. At reduced pressure the particle arrangement undergoes a transition to a liquid and, finally, to an almost gas-like state. During this transition, at first, streamline particle motion around crystalline domains sets in, gradually developing into a more and more irregular particle motion. This transition is also seen in the correlation function $g(r)$ and $g_6(r)$, see Fig. 6.13c,d. The translational as well as the orientational ordering strongly decreases from the ordered state at high pressures to the completely disordered, gas-like state at 39 Pa. The phase transition has been investigated in view of the correlation functions and defect organization [66, 98, 99].

The transition from the ordered to the liquid state is accompanied, and even driven, by the horizontal oscillations of the vertically aligned pairs. One can easily observe these oscillations around the equilibrium position by video microscopy. They are not visible in the trajectories since these are averaged over 10 seconds. The phase transitions occur due to an enormous increase of the dust temperature from essentially room temperature at high gas pressures to about 50 eV at low gas pressures [66]. This dramatic dust heating is driven by the dust oscillations and cannot be explained by simple changes of the plasma parameters with gas pressure. In detailed simulations [100, 101, 102, 103] Schweigert et al. have shown that the particle heating and the phase transitions are driven by an instability due to the nonreciprocal, attractive force, as described in Sec. 6.3.7.2.

6.5.4 Comparison to Colloids

Colloidal suspensions have much in common with dusty plasmas. A colloidal suspension consists of small particles of solid matter that are suspended in a liquid solvent. Paint is a

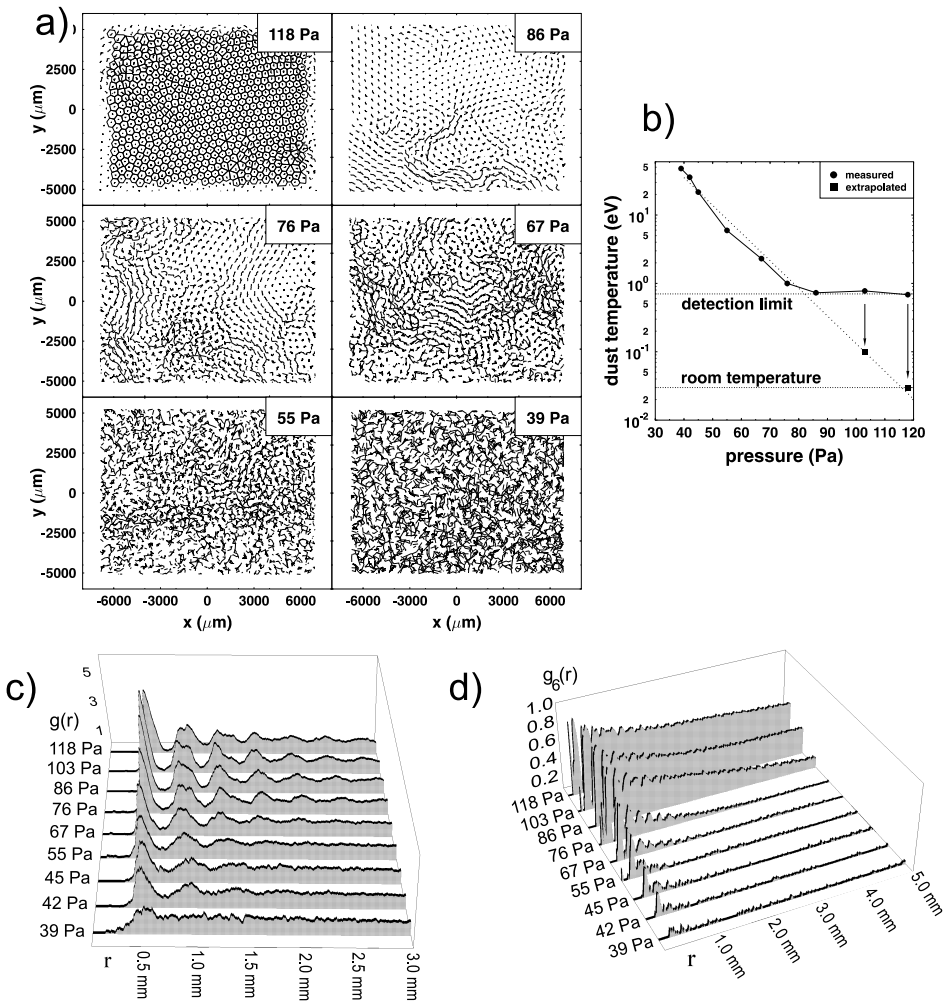

Figure 6.13: a) Trajectories of the dust particles over 10 seconds for decreasing discharge pressure, b) temperature of the dust particles as a function of discharge pressure. A temperature below 0.7 eV could not be detected due to the limited optical resolution, c) pair correlation and d) orientational correlation function versus pressure. After [66].

common example of a colloidal suspension.

Colloidal suspensions that are termed “charge-stabilized colloids” contain particles that become electrically charged by collecting ions from the solvent. This is very analogous to the charging of particles in a dusty plasma. In the colloidal suspension, the solvent contains both

positive and negatively-charged ions, which serve the same roles as ions and electrons in a dusty plasma.

In both dusty plasmas and colloidal suspensions, the medium (plasma or solvent, respectively) is responsible not only for charging the particles, but also for shielding them. The negative and positive ions in the solvent of a colloid arrange themselves spatially so that the electric potential sensed by another charged particle is a screened Coulomb repulsion. The screening is usually characterized by a screening length, or Debye length, λ_{D}. The resulting potential is often a Yukawa potential, see Eq. (6.26). The finite diameter of the particle must be taken into account in modeling the potential, especially for colloidal suspensions where the interparticle spacing is typically as small as the particle diameter.

The medium plays yet another role that is the same for dusty plasmas and colloidal suspensions: damping. For a dusty plasma, the medium is a rarefied gas which contains a small concentration of electrons and ions, and for a colloidal suspension it is a solvent which contains a small concentration of ions. In both cases, the motion of the particle in response to electric fields is impeded by a drag, as the particle must push the surrounding medium in order to move.

The combination of electric repulsion and damping can, in both cases, lead to an ordered structure, like a Wigner lattice. This ordered structure can have properties analogous to the crystalline and liquid phases of molecular matter.

Experimental methods for colloids and dusty plasmas are different in the preparation of the sample, but are similar in the diagnostic methods that are used. The preparation of a colloidal suspension is done by mixing the particles and solvent at atmospheric pressure and temperature. A dusty plasma, on the other hand, is usually made in a vacuum chamber. A colloidal suspension requires no power supply to operate, and can be stored for a long time, whereas a power supply is required to sustain the ionization of the plasma medium so that a dusty plasma will cease to exist as soon as the power supply is turned off. The use of a power supply causes a dusty plasma to be intrinsically a non-equilibrium system, whereas a colloidal suspension is more nearly in thermal equilibrium.

The diagnostics that are similar for colloidal suspensions and dusty plasmas involve imaging and light scattering. Most importantly, in both cases one can uses cameras to view the sample, and record videos of particle motion. With sufficient magnification, one can easily distinguish individual particles. From these videos, one can use computer methods to identify and track the motion of individual particles, as described in another section of this chapter. Particle identification and tracking is most easily done with two-dimensional suspensions, where only a single layer is imaged in the focal plane of a camera. Two-dimensional colloidal suspensions are made by sandwiching the suspension between a pair of glass plates with a small separation, whereas two-dimensional dusty plasmas are usually made by electrical levitation of particles against the downward force of gravity. In colloidal suspensions that are three dimensional, one can use confocal microscopy to view cross-sectional planes within the suspension. By rastering this focal plane, one can assemble a three-dimensional image of the colloidal suspension, assuming that particles do not move significantly. A similar method has been used in dusty plasmas, where a laser sheet for illuminating particles is moved in parallel with a camera that is focused on a plane coinciding with the laser sheet [94, 95].

Gravity can play a significant role in both dusty plasmas and in colloids. In colloidal suspensions, the particles usually have a mass density that is different from the solvent, so

that particles sediment. This sedimentation can be reduced by density-matching the solvent and particles, although doing so limits other choices that would otherwise be available to the experimenter. In a dusty plasma, on the other hand, the medium is a rarefied gas, and there are of course no solid particles that have such a low mass density. Sedimentation is therefore a much more rapid process in a dusty plasma: particles essentially fall like a rock in the absence of an opposing electric field. The role of sedimentation in both dusty plasmas and colloidal suspensions has led experimenters to design experiments that are performed under the weightlessness conditions of space, i.e., microgravity.

Comparing dusty plasmas and colloidal suspensions, some differences are listed below:

- A Coulomb crystal formed with a dusty plasma is much softer than in a colloidal suspension, due to a larger interparticle separation. In a 3D solid state, a dusty plasma suspension has a shear modulus of about $3 \cdot 10^{-9}$ Pa, which is about 10^6 times smaller than for a colloid [104] and 10^{19} times smaller than for metals. This extreme softness allows dusty plasma experimenters to manipulate the entire suspension, to extreme energies if desired, using the radiation pressure applied by a laser beam.

- The particles in a dusty plasma can be underdamped if the gas pressure is reduced sufficiently. In a colloidal suspension, particle motion is overdamped. This difference arises because of the vastly higher mass density of a liquid solvent, as compared to a rarefied gas.

- The particle kinetic temperature in a dusty plasma can be varied, either by relying an instabilities of a multi-layer particle suspension, or laser manipulation. The kinetic temperature of the particles can be varied separately from the temperature of the rarefied gas medium. In a colloidal suspension, the charged particles are in good thermal contact with the solvent, and they will have the same temperature. The colloid experimenter can vary the number density, or volume fraction, of the particles, but not their kinetic temperature.

- In a dusty plasma, the particle suspension cannot come in physical contact with any object or surface. It is necessary to levitate particles using an electric field.

6.6 Waves in Dusty Plasmas

In this section, we will discuss collective effects in the form of waves in dusty plasmas. There is a vast amount of literature on waves in complex plasmas which cannot be covered completely, here. Instead, we will focus on examples of wave types which have been observed in experiments. For a more detailed overview the reader is referred to recent monographs [2, 11].

In general, two categories of waves can be identified, namely those which do not require strong coupling of the dust particles and those which rely on the strong coupling. In the first category, we find, e.g., the dust-acoustic wave (DAW). The dust lattice wave (DLW) with its different “polarizations” requires an ordered dust arrangement on lattice sites and thus belongs to the second category.

6.6.1 Waves in Weakly-Coupled Plasmas: Dust-Acoustic Wave (DAW)

We start with the discussion of waves in weakly coupled dusty plasmas where we like to present an example of an electrostatic wave, the dust acoustic wave [105, 106]. The DAW is a very low-frequent wave with wave frequencies of the order of the dust plasma frequency $\omega_{\rm pd}$ which is much less than the ion plasma and electron plasma frequency ($\omega_{\rm pi}, \omega_{\rm pe}$)

$$\omega_{\rm pd} = \sqrt{\frac{Z_{\rm d}^2 e^2 n_{\rm d0}}{\epsilon_0 m_{\rm d}}} \ll \omega_{\rm pi}, \omega_{\rm pe} \quad , \tag{6.34}$$

where $n_{\rm d0}$ is the equilibrium (undisturbed) dust density. The DAW is a complete analog to the common ion-acoustic wave, where the dust particles take the role of the ions and the ions and electrons take the role of the electrons in the ion-acoustic wave. Thus, the DAW is driven by the electron and ion pressure and the inertia is provided by the massive dust particles.

The dispersion relation of the DAW is given by, see e.g. [107],

$$\omega^2 + i\beta\omega = \frac{\omega_{\rm pd}^2 q^2 \lambda_{\rm Di}^2}{1 + q^2 \lambda_{\rm Di}^2} \tag{6.35}$$

under the (generally justified) assumption of cold dust $T_{\rm d} = 0$ and cold ions $T_{\rm i} \ll T_{\rm e}$ (The full dispersion is given e.g. in [107]). Here, q is the wave vector and $\lambda_{\rm Di}$ is the ion Debye length. In contrast to the common ion-acoustic wave the governing screening length is here the ion Debye length. Second, damping of the wave by friction with the neutral gas is included in terms of the friction coefficient β.

The calculated dispersion relation of the DAW is shown in Fig. 6.14a. For large wave numbers $q\lambda_{Di} \gg 1$ the wave is not propagating and oscillates at the dust plasma frequency $\omega_{\rm pd}$. For long wavelengths $q\lambda_{Di} \ll 1$ the wave is acoustic $\omega = qC_{\rm DAW}$ with the dust-acoustic

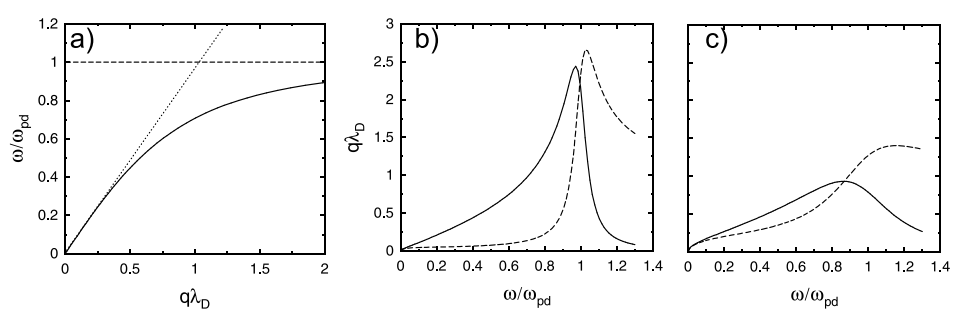

Figure 6.14: a) Dispersion relation of the dust-acoustic wave without damping. The solid line is the full dispersion relation, the dotted line indicates the acoustic limit with the dust-acoustic velocity. b) Dispersion relation with small friction constant $\beta = 0.1\omega_{\rm pd}$ and c) with large friction constant $\beta = 0.5\omega_{\rm pd}$. Here, the solid line refers to the real part of the wave vector and the dashed line to the imaginary part. Note, that in b) and c) the axes have been exchanged with respect to a).

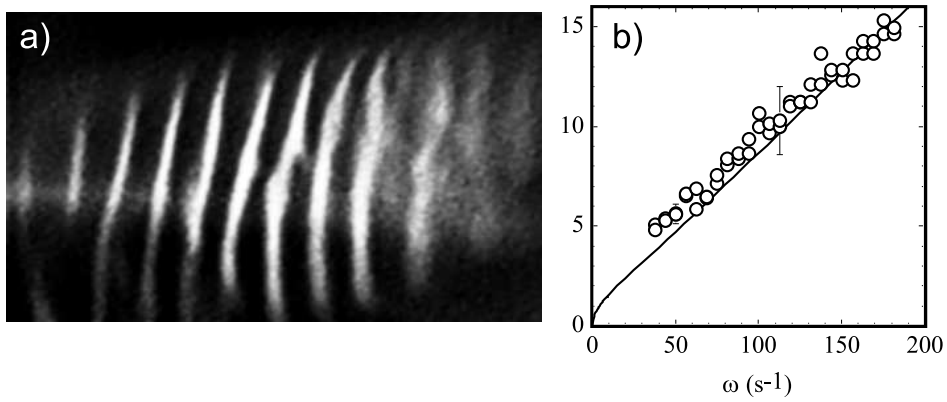

Figure 6.15: a) Observation of the DAW in a DC discharge. The DAW is seen as regions of high and low dust density in scattered light. b) Measured dispersion relation of the DAW. After [72, 108].

wave speed

$$C_{\mathrm{DAW}} = \sqrt{\frac{kT_{\mathrm{i}}}{m_{\mathrm{d}}}\epsilon Z_{\mathrm{d}}^2} \quad . \tag{6.36}$$

As for the ion-acoustic wave, the wave speed is determined by the temperature of the lighter species (T_{i}) and the mass of the heavier m_{d}. In the DAW, the contribution of the high dust charge Z_{d} and the relative dust-to-ion concentration $\epsilon = n_{\mathrm{d}}/n_{\mathrm{i}}$ is retained.

In the experiments, waves are typically excited by an external driver. Thus, in the analysis the wave frequency ω has to be taken as a real value and the wave vector as complex $q = q_{\mathrm{r}} + iq_{\mathrm{i}}$, where the real part q_{r} is related to the wave length and the imaginary q_{i} to the damping length of the wave. Consequently, figure 6.14b and c show the DAW dispersion for small and large values of the friction coefficient β. For small friction the real part of the wave vector behaves similarly to the case of no damping. However, close to $\omega = \omega_{\mathrm{pd}}$ the wave vector turns over and rapidly decreases towards zero. Exactly then, the imaginary part of the wave vector jumps to large values. In the range above ω_{pd}, the dust-acoustic wave is overcritically damped. For larger friction constants (Fig. 6.14c) the wave speed increases and the maximum observable wave number decreases drastically. Moreover, the damping length becomes comparable to the wave length for the entire frequency range and the DAW is found to be strongly damped throughout.

Dust acoustic waves have been observed experimentally in weakly coupled dusty plasmas [72, 108]. There, a dc discharge is driven between an anode disk and the chamber walls. The dust particles are accumulated from a dust tray placed below the anode region. The dust is found to form dust density waves with a certain wavelength and frequency (see Fig. 6.15a). By applying a sinusoidal voltage on the anode the wave can be driven and the dispersion relation is obtained (Fig. 6.15b). The wave shows a linear dispersion in agreement with the DAW.

6.6.2 Waves in Strongly Coupled Dusty Plasmas: Dust Lattice Wave

In this section we will deal with the dust lattice wave and its different polarizations. As the name suggests, the dust lattice wave requires that the particles are arranged in a crystal lattice. Here, we will deal with lattice waves in 2D. Under such conditions the following wave modes can exist: compressional mode, shear mode and transverse mode.

For the compressional (longitudinal) mode, the particle motion is along the wave propagation direction leading to compression and rarefaction. In the shear mode, the dust motion is perpendicular to the wave propagation but in the 2D crystal plane. The transverse mode also describes particle motion perpendicular to the wave propagation, but here the dust motion is an out-of-plane motion and thus requires the consideration of the external confinement of the dust. These three wave types have been observed in the experiment and will be presented in the following.

6.6.2.1 Dispersion Relations of Longitudinal and Shear Modes in 2D

The dispersion relations of 2D hexagonal crystals has been given in [109] without damping. Wang et al. [110] derived the dispersion relations of both modes from a unified perspective by solving the linearized equation of motion analytically. The theory assumes a 2D hexagonal lattice with particles interaction by screened Coulomb repulsion including wave damping. The difference to real experiments is the neglect of thermal motion, defects and particle size distributions.

For waves propagating parallel to one of the primitive translation vectors the dispersion relation for both longitudinal and shear modes are expressed as [110]

$$\omega_l^2 + i\beta\omega_l = \frac{1}{\pi}\sum_{x,y} F(X,Y)\sin^2\left(\frac{qX}{2}\right) \tag{6.37}$$

$$\omega_s^2 + i\beta\omega_s = \frac{1}{\pi}\sum_{x,y} F(Y,X)\sin^2\left(\frac{qX}{2}\right) \quad , \tag{6.38}$$

where the summation is carried out over all particles in the 2D lattice. The frequencies ω and β are normalized by ω_{pd}, and the equilibrium particle position X, Y and q are normalized by the interparticle distance b. Here, ω_{pd} is defined as

$$\omega_{\mathrm{pd}} = \sqrt{\frac{Z_{\mathrm{d}}^2 e^2}{\epsilon_0 m_{\mathrm{d}} b^3}} \tag{6.39}$$

which can be taken as the dust plasma frequency in the case of a crystalline arrangement. The function $F(X,Y)$ represents the spring constant matrix which is given by [110, 65, 111]

$$F(X,Y) = \frac{1}{R^5} e^{-\kappa R}\left[X^2(3+3\kappa R+\kappa^2 R^2) - R^2(1+\kappa R)\right] \quad , \tag{6.40}$$

where $R^2 = X^2 + Y^2$ and $\kappa = b/\lambda_{\mathrm{D}}$. The spring matrix comes from the Taylor expansion of the screened Yukawa particle interaction around the particle distance b. The dispersion relation of the compressional and shear mode are shown in Fig. 6.16. For finite values of κ,

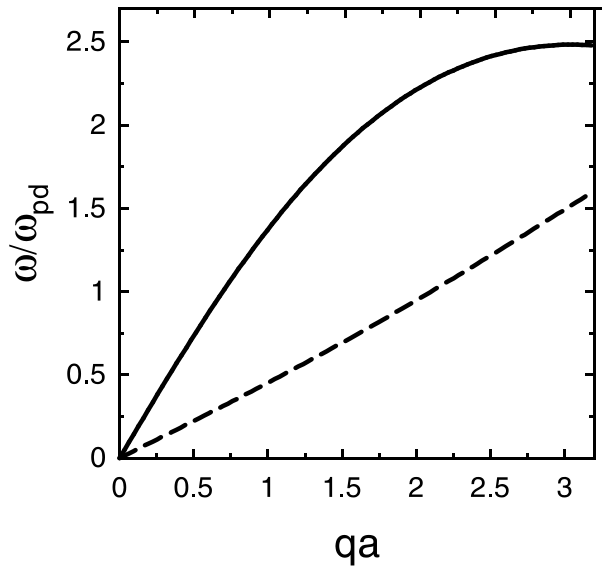

Figure 6.16: Dispersion relation of a 2D dust lattice wave without damping. The solid line is the compressional mode and the dashed line is the shear mode for $\kappa = 2$.

both modes are acoustic in the long wavelength limit, i.e. $\omega \propto q$ for $q \to 0$. The sound speeds of the two modes are then $c_{l,s} = \omega_{l,s}/q$ (for $q \to 0$). The sound speed of the compressional mode is much larger than that of the shear mode. For shorter wavelengths the compressional mode shows a strong dispersive nature whereas the shear mode is nearly acoustic for all q.

6.6.2.2 Measurements of Compressional and Shear Dust Lattice Waves

The 1D and 2D compressional dust lattice wave has been identified and measured in experiments of Homann et al. [112, 111]. There, the waves have been excited by a focused laser beam. In the 2D case, the laser beam of a Argon ion laser was expanded into a line and focused onto the first row of particles in a 2D plasma crystal. By periodic modulation of the laser power a plane wave was launched in the plasma crystal (see Fig. 6.17a). The wave motion of the dust was analyzed in terms of the phase (Fig. 6.17b) and amplitude (Fig. 6.17c) of the dust particles as a function of distance from the excitation region. As in the case of the DAW, the wave frequency ω has to be taken as real in the analysis of the experiment and the wave vector q as complex. The phase dependence directly results in the wavelength λ and the amplitude decrease in a damping length L for that excitation frequency. Finally, the real part of the wave vector is derived from the wavelength as $q_{\mathrm{r}} = 2\pi/\lambda$ and the imaginary part from the damping length as $q_{\mathrm{i}} = 1/L$ (Fig. 6.17d,e). The measured dispersion relation is then compared to the compressional 2D dispersion relation of Eq. 6.37.

Using more advanced excitation techniques, Nunomura et al. [65] have measured both shear and compressional waves in great detail by laser excitation (see Fig. 6.18). They suc-

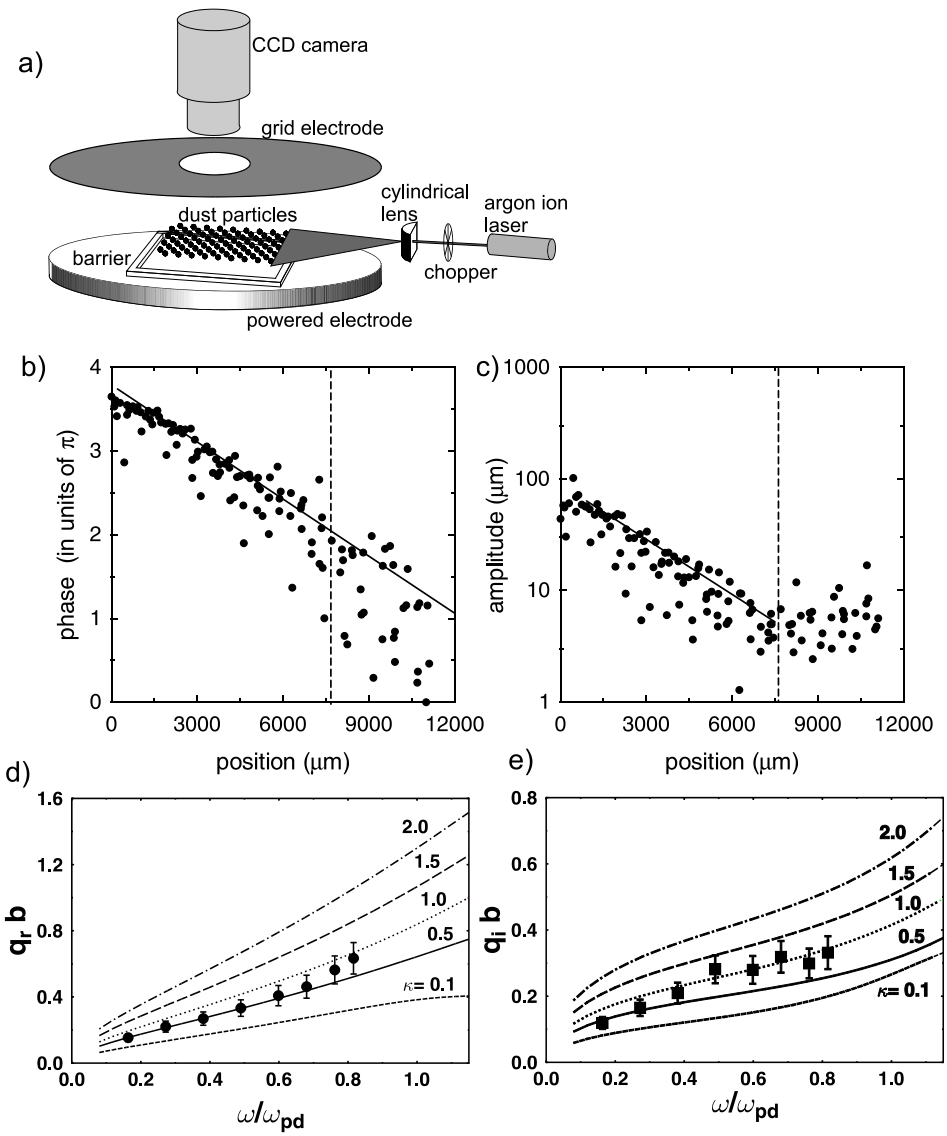

Figure 6.17: a) Scheme of the experimental setup for the excitation of 2D dust lattice waves. b) Phase and c) amplitude of the dust particle motion as a function of distance from the excitation region for an excitation frequency of 2.8 Hz. d) and e) Real and imaginary wave vector as a function of frequency. The symbols denote the experimental data. The lines indicate the dispersion relation of the 2D DLW for various values of the screening strength κ. After [111].

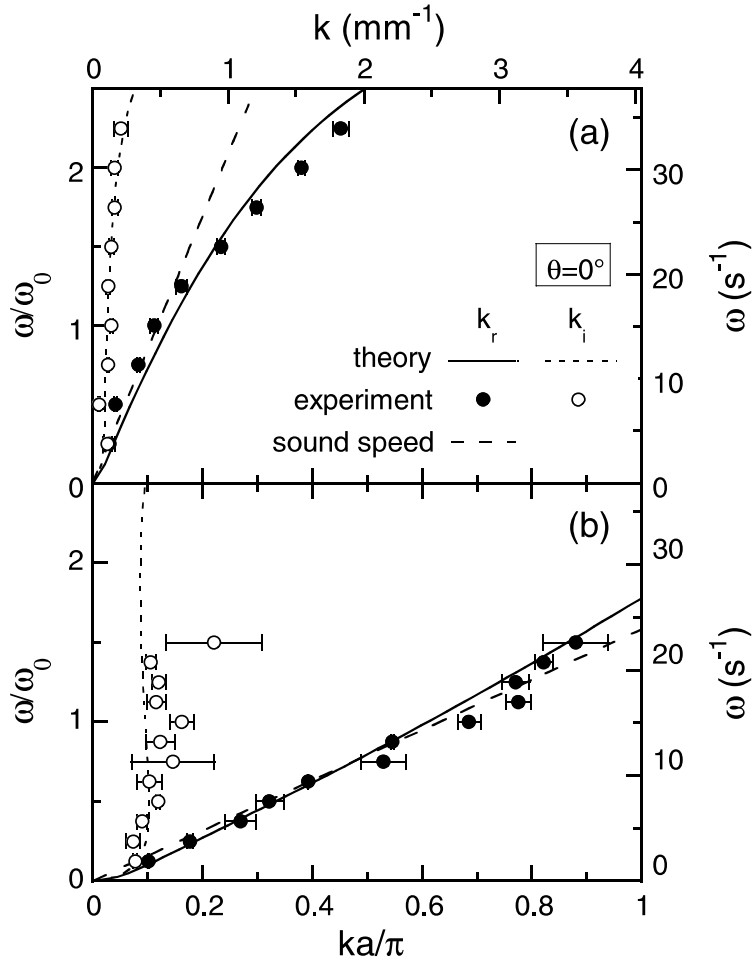

Figure 6.18: Dispersion relations of (a) the longitudinal and (b) the transverse waves in a hexagonal monolayer crystal. A dispersive characteristic is seen for the longitudinal wave at high wave frequency ω while the transverse wave shows a linear dispersion over a wide range of wave vectors k. The data were obtained for wave propagation along one of the principal lattice vectors of the hexagonal lattice. The closed and open symbols are experimental data for $k_{\mathrm{r}}(= q_{\mathrm{r}})$ and $k_{\mathrm{i}}(= q_{\mathrm{i}})$, respectively. The solid and dashed lines are calculated from the Eq. 6.37.

ceeded in exciting and analyzing the wave propagation along different lattice orientations in 2D hexagonal crystals and found good agreement with the theoretical DLW dispersion relation.

Fitting the theoretical dispersion relations to the measured compressional and shear modes yields reliable values for the dust plasma frequency ω_{pd} and the screening strength κ. From the dust plasma frequency, readily the dust charge Z_{d} is derived. Waves are therefore a pow-

erful tool to measure the crucial parameters of dusty plasmas with good accuracy. The dust particle charge obtained from the wave dispersion is of the order of 10^4 elementary charges for particles of 10 microns diameter which in agreement with the vertical resonance method and is compatible with the OML model. The screening strength $\kappa = b/\lambda_{\mathrm{D}}$ is found to be of the order of unity. This means, that interparticle distance and shielding length are comparable. With typical interparticle distances of some hundred microns the observed shielding length is of the order of the electron Debye length.

6.6.2.3 Mach Cones

An alternative method to derive the sound speed in plasma crystals is the excitation of Mach cones. Mach cones are produced by objects that move through a medium with a velocity faster than the wave speed in that medium. This phenomenon is known, e.g. from the sonic boom behind a plane at supersonic velocity. Similarly, Mach cones can be observed in dusty plasmas when an object moves faster than the acoustic speed of the DLW in these systems. Mach cones in dusty plasmas have first been observed by Samsonov et al. [113, 114]. There, dust particles which accidentally are trapped below the actual 2D plasma crystal are found to move at large, supersonic, speeds at low gas pressure. The disturbance by these lower particles introduces a Mach cone in the upper plasma crystal.

Melzer et al. [115] have generated Mach cones in plasma crystals using laser manipulation. There, the focus of a laser beam was swept at a velocity $V > c_l$ through the crystal using a moving galvanometer scanning mirror (Fig. 6.19). The laser technique allows the formation of Mach cones in a repetitive and controllable manner. The Mach cone has an opening angle μ that satisfies the Mach cone relation

$$\sin \mu = \frac{c_l}{V} \quad . \tag{6.41}$$

Thus from the opening angle μ the sound speed of the DLW is readily obtained. Figure 6.19b shows the Mach cone observed by the laser manipulation technique. A strong first Mach cone is easily seen. However, also additional secondary and tertiary Mach cones are also observable. These additional features arise from the dispersive characteristics of the DLW at shorter wavelengths [116]. Like the wave pattern of a moving ship, these features can be interpreted as interference patterns of the wave packages launched by the moving laser beam.

The Mach cone in Fig. 6.19 is a compressional Mach cone due to excitation of compressional waves. Mach cones due to shear waves have been demonstrated by Nosenko et al. [117]. These shear Mach cones can be observed at much lower velocities V due to the much smaller acoustic velocity of the shear waves.

Mach cones have been predicted to occur in the rings of Saturn and should be detectable by the Cassini spacecraft that has arrived at Saturn in 2004 [118]. In Saturn's rings, large boulders moving in Keplerian orbits are likely to have supersonic speeds with respect to smaller dust particles which moves at speeds determined by their electrostatic interactions with Saturn's plasma environment.

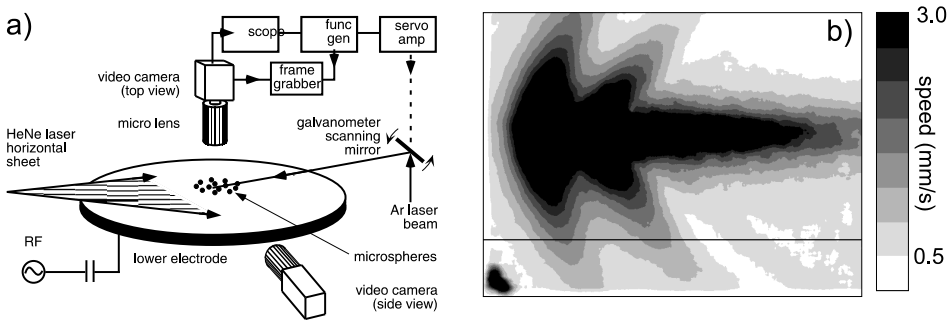

Figure 6.19: Mach cones in dusty plasmas. a) Scheme of the experimental setup for the excitation of a compressional Mach cone, b) gray scale map of the particle velocities in the compressional Mach cone. After [115].

6.6.2.4 Transverse Dust Lattice Waves

Finally, transverse dust lattice waves will be demonstrated, here. In this wave mode, the particle motion is perpendicular to the wave propagation, and also out-of-plane, i.e. in the vertical direction for typical plasma crystals. Such out-of-plane elongations are only stable due to the presence of a confinement potential. Otherwise the particles would just move away from each other due to their Coulomb repulsion. The dispersion of the transverse DLW is readily obtained as [119]

$$\omega^2 + i\beta\omega = \omega_0^2 - \frac{1}{\pi}\omega_{\mathrm{pd}}^2 \sum_{\ell=1}^{M} \frac{e^{-\ell\kappa}}{\ell^3}\,(1+\ell\kappa)\sin^2\left(\frac{\ell q b}{2}\right) \quad . \tag{6.42}$$

Here, the influence of many neighboring particles is included in the sum over ℓ. Here, $M = 1$ includes the interaction of nearest neighbors only, $M = 2$ also includes the interaction of next-nearest neighbors etc. One can see that the influence of the vertical confinement ω_0^2 is necessary to yield a stable dispersion relation. It is interesting to note that this wave is a backward ($\partial\omega/\partial q < 0$) and "optical" wave, i.e. $\omega \to \omega_0$ for $q \to 0$.

Misawa et al. [120] investigated vertical oscillations which propagate along a 1D chain of particles. The authors have determined part of the dispersion relation where a finite frequency is found for $q \to 0$ and the dispersion also has a negative slope, as expected for the transverse DLW. However, the overall agreement of the measured and the theoretical dispersion was not satisfying.

6.6.2.5 Natural Phonons

Meanwhile, image analysis techniques are advanced enough to determine the dispersion relation of waves from the naturally excited lattice oscillations (phonons). The particles in a dusty plasma exhibit a Brownian motion that is excited by thermal or electrostatic fluctuations in the plasma. This small-amplitude motion is sufficient to reconstruct the wave spectrum in the system [121]. Thereby it is assumed that the Brownian motion is a random superposition of all

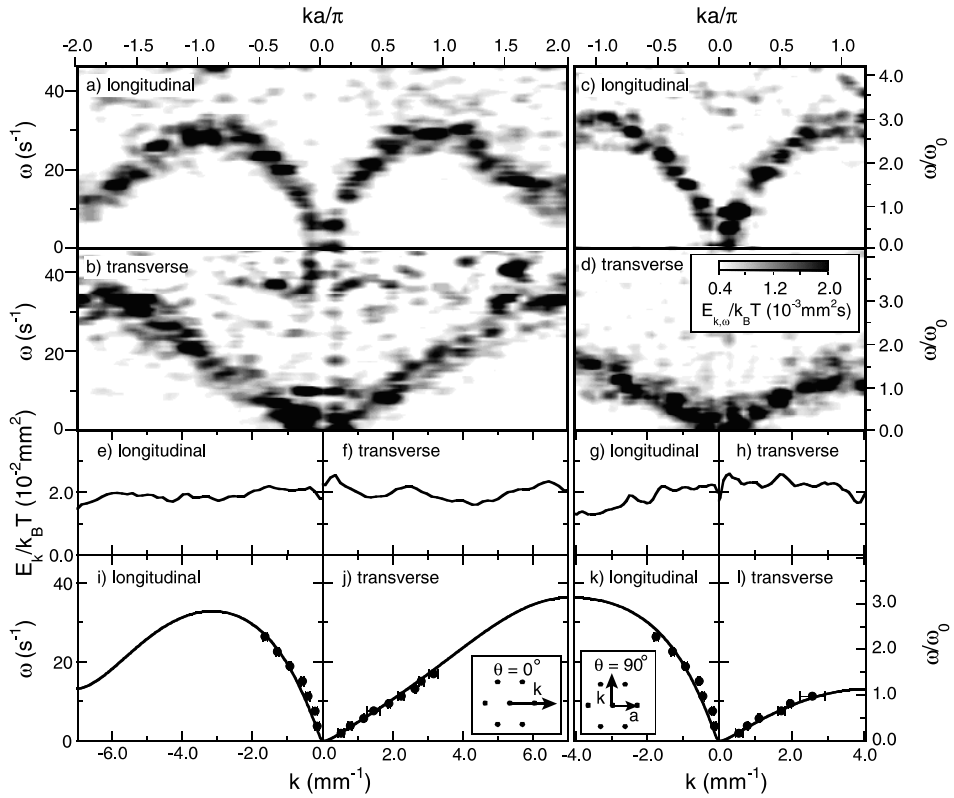

Figure 6.20: Phonons in the first Brillouin zone of a monolayer hexagonal crystal. (a)-(d) Spectra of the wave energy density (Eq. 6.44) in the $\vec{k}$-ω space ($\vec{k} = \vec{q}$ in our notation) obtained from the Brownian motion of the particles. Darker grays correspond to higher wave energy. Energy is concentrated along a curve corresponding to a dispersion relation. (e)-(h) Spectra integrated over ω, showing that the wave energy is distributed nearly uniformly with respect to wave number. (i)-(l) Theoretical dispersion relation (curves) fitted to the experimental dispersion relation for waves excited intentionally using a laser (circles). The angle θ between $\vec{k}$ and the principal lattice vector in the hexagonal lattice is 0° in the left panels, 90° in the right panels.

possible wave modes. Then, the wave spectrum is reconstructed from the Fourier transform of the particle velocities $\vec{v}(\vec{r}, t)$ by

$$V(\vec{q}, \omega) = \frac{2}{TL} \int_0^T \int_0^L \vec{v}(\vec{r}, t) e^{-i(\vec{q}\cdot\vec{r} - \omega t)} \, d\vec{r} \, dt \quad . \tag{6.43}$$

The spectral power density $S(\vec{q}, \omega)$ is a measure of the energy of the wave mode with

$$S(\vec{q}, \omega) = \frac{1}{2} m_{\mathrm{d}} \left| V(\vec{q}, \omega) \right|^2 \quad . \tag{6.44}$$

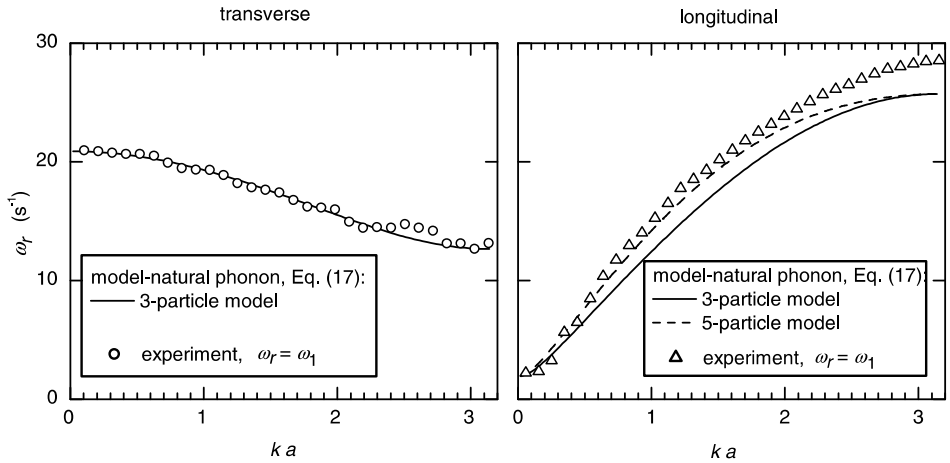

Figure 6.21: Dispersion relations for natural phonons obtained in a linear chain of $N = 28$ particles. Symbols denote experimental values, the solid and dashed lines are theoretical curves including 3 ($M = 1$) or 5 ($M = 2$) nearest-neighbor interactions. After [68].

In Fig. 6.20 the phonon spectrum of the compressional and shear wave in a monolayer crystal obtained from the Brownian motion is shown. Indeed, the maximum of the power density precisely reflects the dispersion relation of the wave modes. The wave dispersion is exactly recovered from the random motion. Moreover, the energy stored in the wave is evenly distributed over the range of wave vectors indicating that the principle of equipartition of the energy holds, here.

Longitudinal and transverse dust lattice waves in 1D chains have been analyzed by Liu et al. [122, 68]. In a linear chain configuration they have measured the wave spectrum from laser excited and from natural, thermally excited modes, see Fig. 6.21. There, the tranverse mode is due to horizontal particle motions perpendicular to the chain and longitudinal modes are motions along the chains. In addition, also the longitudinal modes in the chain have been determined. The transverse mode indeed was found to be an optical, backward wave. The measured wave spectrum was in very good agreement with both the longitudinal and transverse dispersion.

This technique is now widely applied in dusty plasmas to study e.g. waves in solid and liquid phases [123], longitudinal and transverse modes in linear chains [68] or in finite particle systems [70].

6.6.3 Finite Clusters and Normal Modes

After the discussion of waves in infinite systems, we now like to briefly address finite systems of dust particles, so-called dust or Coulomb clusters.

6.6.3.1 2D Clusters

In 2D clusters, only a small number of dust particles, say $N = 1$ to 500, is trapped in the sheath above the lower electrode with additional horizontal confinement (see Sec. 6.4.1). Detailed investigations have been performed for 2D isotropic clusters (see Fig. 6.7b) where a circular parabolic confinement is used.

Under the interplay of horizontal parabolic confinement and Coulomb repulsion the particles arrange in concentric shells (see also Fig. 6.22). The structure and their dynamic properties dramatically depends on the particle number N. Like in atomic and nuclear physics there exist "magic" particle numbers of strong dynamic stability, e.g. the N=19 (1,6,12) cluster. The notation $(N_1, N_2, N_3, \ldots)$ describes N_1 particles in the inner ring, N_2 in the second and so on. Such structures have indeed been considered as a possible model of the atom by J.J. Thomson in 1904 [124]. Finite Coulomb clusters are also observed in colloidal suspensions [125], in quantum dots [126], and electrons on liquid helium [127].

The finite clusters are described in terms of the total energy

$$E = \frac{1}{2} m_{\mathrm{d}} \omega_{\mathrm{h}}^2 \sum_{i=1}^{N} r_i^2 + \frac{Z_{\mathrm{d}}^2 e^2}{4\pi\epsilon_0} \sum_{i>j}^{N} \frac{\exp(-r_{ij}/\lambda_{\mathrm{D}})}{r_{ij}} \quad , \tag{6.45}$$

where $\vec{r}_i = (x_i, y_i)$ is the position of the i-th particle in the horizontal plane and $r_{ij} = |\vec{r}_i - \vec{r}_j|$.

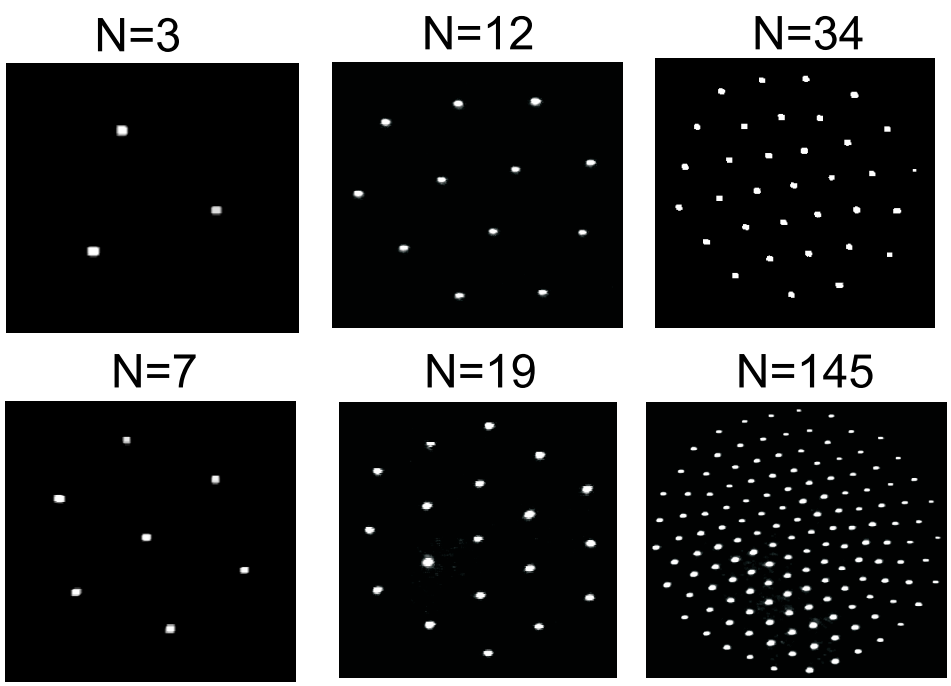

Figure 6.22: Experimental realizations of finite clusters in dusty plasmas with $N = 3$, 7, 19, 20, 34 and 145 particles. After [70].

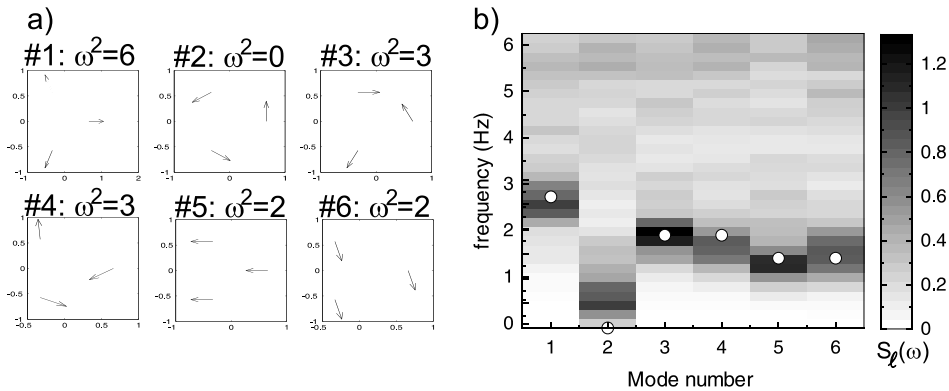

Figure 6.23: a) The 6 eigen modes of a $N = 3$ cluster with the corresponding mode frequencies ω^2 (in units of $\omega_{\rm h}^2/2$). b) Spectral power density of the 3 particle cluster derived from the thermal motion of the particles. The white dots indicate the best-fit theoretical values of the mode frequencies. After [70].

The first term is the potential energy due to the horizontal confinement (with resonance frequency $\omega_{\rm h}$) and the second is the Coulomb repulsion of the particles.

The equilibrium structure of these systems is derived from the minimum of the total energy [128, 129, 130]. Experimentally they have been observed by Juan et al. [131], Klindworth et al. [132] and Melzer et al. [69, 70]. The observed cluster structure is usually in perfect agreement with the theoretical predictions. The particles form concentric shells and the occupation number in the shells correspond to those expected from simulations.

The dynamic properties of finite clusters are described in terms of their normal modes which replace the dispersion relation of infinite systems. The normal modes are obtained from the dynamical matrix $\mathbf{A}$

$$\mathbf{A} = \begin{pmatrix} \dfrac{\partial^2 E}{\partial x_i \partial x_j} & \dfrac{\partial^2 E}{\partial x_i \partial y_j} \\ \dfrac{\partial^2 E}{\partial y_i \partial x_j} & \dfrac{\partial^2 E}{\partial y_i \partial y_j} \end{pmatrix} \tag{6.46}$$

where the second derivative constructions are themselves $1N \times 1N$ matrices that contain the possible combinations of i and j. The eigen values and eigen vectors of $\mathbf{A}$ describe the normal mode oscillations of the finite clusters. The eigen values are the oscillation frequencies and the eigen vectors describe the mode oscillation patterns.

This is demonstrated for the simple case of $N = 3$ particles in Fig. 6.23a where the $2N = 6$ eigen modes are presented. Modes that always occur in 2D clusters are two center-of-mass modes (i.e. oscillations of the entire cluster in the horizontal confining potential, modes number 5 and 6), the rotation of the entire cluster (mode number 2) and the breathing mode (i.e. coherent purely radial motion of all particles, mode number 1). For the 3-particle cluster also two “kink” modes are found (mode number 3 and 4).

The normal mode spectrum of dust clusters is derived in analogy to the wave spectrum from the thermal Brownian motion of the dust particles [70]. The power spectrum of mode

number ℓ is obtained from

$$S_\ell(\omega) = \frac{2}{T}\left|\int_0^T \sum_{i=1}^N \vec{v}_i(t)\cdot\vec{e}_{i,\ell}\, e^{i\omega\, t} dt\right|^2 \quad , \tag{6.47}$$

where $\vec{e}_{i,\ell}$ is the eigen vector for particle i in mode number ℓ. Here, the eigen vectors in the finite cluster take the role of the wave vector in the dispersion in infinite systems. For the 3-particle cluster the power spectrum is shown in Fig. 6.23b). The observed power spectrum is in very good agreement with the expected mode frequencies. This technique can be applied to clusters of any size and has been demonstrated for clusters with several hundred particles [70, 133].

Moreover, also the stability of the cluster ("magic number" configurations) can be judged from the power spectrum. The mode with the lowest eigen frequency (besides cluster rotation) determines the stability of the cluster. If the eigen frequency is close to zero this mode is easily excited and can lead to changes in configuration. Typically, the lowest eigen frequency mode for small clusters is the intershell rotation where two cluster rings show differential rotation. E.g. for the 19-particle cluster, which is a "magic number" configuration due to its high symmetry, the intershell rotation frequency can hardly be excited [132].

6.6.3.2 3D Clusters: Coulomb Balls

Clusters in a three-dimensional confinement (see Fig. 6.7) also arrange in highly ordered structures. The systems form concentric spheres, arranged like "onion shells" [134]. Recently, a major breakthrough in the confinement of dust clusters has been achieved [48]. It has become possible to confine 3D dust clusters in a potential that obviously is isotropic and that does not

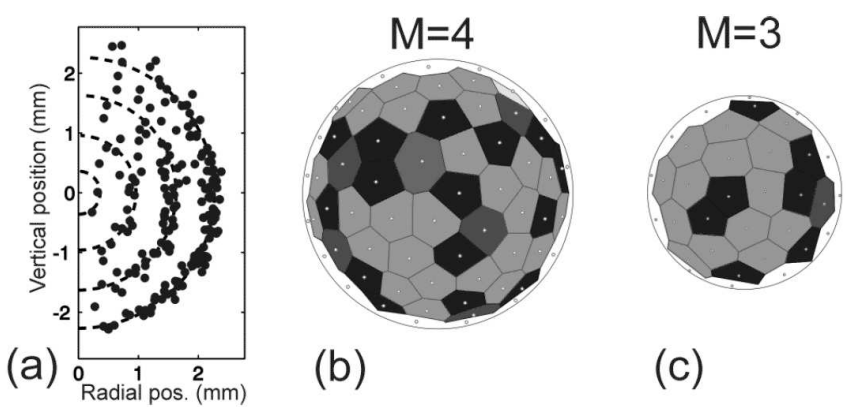

Figure 6.24: 3D dust cluster in an experiment with $N = 190$ particles. a) plot of the radial coordinate $\rho = \sqrt{x^2 + y^2}$ versus the vertical coordinate z. The cluster is seen to have 4 shells. b) Voronoi analysis of the outer (4th) shell and c) of the 3rd shell. Pentagons are marked dark grey, hexagons are light grey. Defect polygons with more than 6 nearest neighbors are colored medium-grey. After [48].

lead to void formation. The confinement has been achieved using the combined interaction of thermophoretic levitation and a horizontal boundary due to glass walls.

An experimental dust cluster is shown in Fig. 6.24. The cluster consists of $N = 190$ particles and is arranged in 4 concentric shells in a $(2, 21, 60, 107)$ configuration. The structure within each shell consist of hexagons and pentagons. A certain number of pentagons is needed to ensure the curvature of the sphere and to form closed shells. But also some defects, i.e. particles with more than 6 nearest neighbors are found.

The investigation of the 3D clusters is just at its beginning. Up to now, information have been revealed on the structure of these systems. The dynamical properties are not explored so far. However, the study of these systems will be one of the challenging and promising future directions in dusty plasma physics.

6.7 Concluding Remarks

We have given a brief survey of experiments in dusty plasmas. We have focused on the fundamental properties of dusty plasmas like particle charging, interaction potentials and forces as well as strong-coupling effects and waves.

To summarize, the main properties of dusty plasmas compared to "usual" plasmas are compiled below

- Dusty plasmas are at least three component plasmas (electrons, ions and dust). In this sense, dusty plasmas are comparable to negative ion plasmas.

- The typical charge on the charge carriers (dust) are of the order of 10 000 elementary charges which leads to strong coupling.

- The dust charge is variable and depends on the local plasma parameters. Thus, the charge becomes a dynamic variable.

- The dust mass is by orders of magnitudes larger than that of electrons and ions. Thus the dominant time scale is that of the dust plasma frequency ω_{pd} which is by orders of magnitude smaller than that of electrons and ions leading to convenient time scales for the observation of dynamic processes.

- The slow time scales allow that electrons *and* ions contribute to shielding which should results in different shielding scales.

- The dust size is not negligibly small leading to surface phenomena and forces which are unimportant in "usual" plasmas.

All of these unique properties of dusty plasmas an number of new phenomena occur in dusty plasmas like new force, new types of waves, crystallization processes, phase transitions, observation of processes on the kinetic level and many more. The authors hope that they have clarified the origin of these phenomena and that they have demonstrated why dusty plasmas have become one of the very interesting fields in plasma physics.

References

[1] C. K. Goertz, Rev. Geophys. **27**, 271 (1989).

[2] F. Verheest, *Waves in Dusty Space Plasmas* (Kluver Academic Publishers, Dordrecht, 2000).

[3] G. S. Selwyn, J. E. Heidenreich, and K. L. Haller, J. Vac. Sci. Technol. A **9**, 2817 (1991).

[4] *Dusty Plasmas*, edited by A. Bouchoule (John Wiley & Sons, Chichester, 1999).

[5] J. H. Chu and L. I, Phys. Rev. Lett. **72**, 4009 (1994).

[6] H. Thomas *et al.*, Phys. Rev. Lett. **73**, 652 (1994).

[7] D. H. E. Dubin and T. M. O'Neill, Rev. Mod. Phys. **71**, 87 (1999).

[8] N. A. Clark, A. J. Hurd, and B. J. Ackerson, Nature **281**, 57 (1979).

[9] P. Pieranski, Contemp. Phys. **24**, 25 (1983).

[10] A. Piel and A. Melzer, Plasma Phys. Control. Fusion **44**, R1 (2002).

[11] P. K. Shukla and A. A. Mamun, *Introduction to Dusty Plasma Physics* (Institute of Physics Publishing, Bristol, 2002).

[12] V. E. Fortov *et al.*, Physics Reports **421**, 1 (2005).

[13] C. M. C. Nairn, B. M. Annaratone, and J. Allen, Plasma Sources Sci. Technol. **7**, 478 (1998).

[14] I. B. Bernstein and I. N. Rabinowitz, Phys. Fluids **2**, 112 (1959).

[15] F. F. Chen, Plasma Phys. **7**, 47 (1965).

[16] E. C. Whipple, Rep. Prog. Phys. **44**, 1198 (1981).

[17] I. H. Hutchinson, Plasma Phys. Control. Fusion **45**, 1477 (2003).

[18] I. H. Hutchinson, New J. Phys. **6**, 43 (2004).

[19] I. H. Hutchinson, Plasma Phys. Control. Fusion **47**, 71 (2005).

[20] J. L. Spitzer, *Physical Processes in the Interstellar Medium* (John Wiley, New York, 1978).

[21] C. Cui and J. Goree, IEEE Trans. Plasma Sci. **22**, 151 (1994).

[22] O. Havnes, T. K. Aanesen, and F. Melandsø, J. Geophys. Res. **95**, 6581 (1990).

[23] L. Boufendi *et al.*, Appl. Phys. Lett. **60**, 169 (1992).

[24] N. Meyer-Vernet, Astronom. Astrophys. **105**, 98 (1982).

[25] V. W. Chow, D. A. Mendis, and M. Rosenberg, IEEE Trans. Plasma Sci. **22**, 179 (1994).

[26] J. Goree, Phys. Rev. Lett. **69**, 277 (1992).

[27] S. J. Choi and M. J. Kushner, IEEE Trans. Plasma Sci. **22**, 138 (1994).

[28] M. Lampe, V. Gavrishchaka, G. Ganguli, and G. Joyce, Phys. Rev. Lett. **86**, 5278 (2001).

[29] S. Hamaguchi and R. T. Farouki, Phys. Rev. E **49**, 4430 (1994).

[30] H. C. Lee and B. Rosenstein, Phys. Rev. E **55**, 7805 (1997).

[31] G. Lapenta, Phys. Rev. Lett. **75**, 4409 (1995).

[32] U. Mohideen *et al.*, Phys. Rev. Lett. **81**, 349 (1998).

[33] T. G. Northrop and T. J. Birmingham, Planet. Space Sci. **38**, 319 (1990).

[34] M. S. Barnes *et al.*, Phys. Rev. Lett. **68**, 313 (1992).

[35] M. D. Kilgore, J. E. Daugherty, R. K. Porteous, and D. B. Graves, J. Appl. Phys. **73**, 7195 (1993).

[36] J. Perrin, P. Molinàs-Mata, and P. Belenguer, J. Phys. D: Appl. Phys. **27**, 2499 (1994).

[37] X. Chen, J. Phys. D: Appl. Phys. **29**, 995 (1996).

[38] F. F. Chen, *Introduction to Plasma Physics and controlled Fusion* (Plenum Press, New York London, 1984), Vol. 1. Plasma Physics.

[39] S. Khrapak, A. V. Ivlev, G. Morfill, and H. Thomas, Phys. Rev. E **66**, 046414 (2002).

[40] S. Khrapak, A. V. Ivlev, G. Morfill, and S. Zhdanov, Phys. Rev. Lett. **90**, 225002 (2003).

[41] I. V. Schweigert, A. L. Alexandrov, and F. M. Peeters, IEEE Trans. Plasma Sci. **32**, 623 (2004).

[42] A. Ivlev, S. A. Khrapak, S. Zhdanov, and G. Morfill, Phys. Rev. Lett. **92**, 205007 (2004).

[43] C. Zafiu, A. Melzer, and A. Piel, Phys. Plasmas **10**, 1278 (2003).

[44] V. Yaroshenko *et al.*, Phys. Plasmas **12**, 093503 (2005).

[45] H. Vestner and L. Waldmann, Physica **86A**, 303 (1977).

[46] G. M. Jellum, J. E. Daugherty, and D. B. Graves, J. Appl. Phys. **69**, 6923 (1991).

[47] H. Rothermel *et al.*, Phys. Rev. Lett. **89**, 175001 (2002).

[48] O. Arp, D. Block, A. Piel, and A. Melzer, Phys. Rev. Lett. **93**, 165004 (2004).

[49] P. S. Epstein, Phys. Rev. **23**, 710 (1924).

[50] B. Liu, J. Goree, V. Nosenko, and L. Boufendi, Phys. Plasmas **10**, 9 (2003).

[51] A. Ashkin, Phys. Rev. Lett. **24**, 156 (1970).

[52] A. Melzer, Plasma Sources Sci. Technol. **10**, 303 (2001).

[53] U. Konopka, G. Morfill, and L. Ratke, Phys. Rev. Lett. **84**, 891 (2000).

[54] T. Trottenberg, A. Melzer, and A. Piel, Plasma Sources Sci. Technol. **4**, 450 (1995).

[55] S. V. Vladimirov and M. Nambu, Phys. Rev. E **52**, 2172 (1995).

[56] M. Nambu, S. V. Vladimirov, and P. K. Shukla, Phys. Lett. A **203**, 40 (1995).

[57] F. Melandsø and J. Goree, Phys. Rev. E **52**, 5312 (1995).

[58] O. Ishihara and S. V. Vladimirov, Phys. Plasmas **4**, 69 (1997).

[59] G. Joyce, M. Lampe, and G. Ganguli, Phys. Rev. Lett. **88**, 095006 (2002).

[60] A. Melzer, V. Schweigert, and A. Piel, Phys. Rev. Lett. **83**, 3194 (1999).

[61] A. Melzer, V. Schweigert, and A. Piel, Physica Scripta **61**, 494 (2000).

[62] V. A. Schweigert *et al.*, Phys. Rev. E **54**, 4155 (1996).

[63] A. Melzer *et al.*, Phys. Rev. E **54**, 46 (1996).

[64] K. Takahashi *et al.*, Phys. Rev. E **58**, 7805 (1998).

[65] S. Nunomura *et al.*, Phys. Rev. E **65**, 066402 (2002).

[66] A. Melzer, A. Homann, and A. Piel, Phys. Rev. E **53**, 2757 (1996).

[67] B. Liu, K. Avinash, and J. Goree, Phys. Rev. E **69**, 036410 (2004).

[68] B. Liu and J. Goree, Phys. Rev. E **71**, 046410 (2005).

[69] A. Melzer, M. Klindworth, and A. Piel, Phys. Rev. Lett. **87**, 115002 (2001).

[70] A. Melzer, Phys. Rev. E **67**, 016411 (2003).

[71] V. E. Fortov *et al.*, Phys. Plasmas **7**, 1374 (2000).

[72] A. Barkan, R. L. Merlino, and N. D'Angelo, Phys. Plasmas **2**, 3563 (1995).

[73] E. Thomas, Phys. Plasmas **9**, 17 (2002).

[74] N. Sato *et al.*, Phys. Plasmas **8**, 1786 (2001).

[75] J.-L. Dorier, C. Hollenstein, and A. Howling, J. Vac. Sci. Technol. A **13**, 918 (1995).

[76] G. Praburam and J. Goree, Plasma Sources Sci. Technol. **5**, 84 (1996).

[77] J. Goree, G. Morfill, V. Tsytovich, and S. V. Vladimirov, Phys. Rev. E **59**, 7055 (1999).

[78] V. Tsytovich, S. V. Vladimirov, G. Morfill, and J. Goree, Phys. Rev. E **63**, 056609 (2001).

[79] A. Melzer, T. Trottenberg, and A. Piel, Phys. Lett. A **191**, 301 (1994).

[80] P. Belenguer, These de doctorat (in French), Université Nancy I (1990).

[81] T. J. Sommerer, W. N. G. Hitchon, R. E. P. Harvey, and J. E. Lawler, Phys. Rev. A **43**, 4452 (1991).

[82] P. Belenguer *et al.*, Phys. Rev. A **46**, 7923 (1992).

[83] E. Tomme, D. Law, B. M. Annaratone, and J. Allen, Phys. Rev. Lett. **85**, 2518 (2000).

[84] A. Homann, A. Melzer, and A. Piel, Phys. Rev. E **59**, 3835 (1999).

[85] E. Tomme, B. M. Annaratone, and J. Allen, Plasma Sources Sci. Technol. **9**, 87 (2000).

[86] H. Schollmeyer, A. Melzer, A. Homann, and A. Piel, Phys. Plasmas **6**, 2693 (1999).

[87] A. Ivlev *et al.*, Phys. Rev. Lett. **85**, 4060 (2000).

[88] C. Zafiu, A. Melzer, and A. Piel, Phys. Rev. E **63**, 066403 (2001).

[89] S. Nunomura, T. Misawa, N. Ohno, and S. Takamura, Phys. Rev. Lett. **83**, 1970 (1999).

[90] S. Ichimaru, Rev. Mod. Phys. **54**, 1017 (1982).

[91] S. Hamaguchi, R. Farouki, and D. H. E. Dubin, Phys. Rev. E **56**, 4671 (1997).

[92] P. Hartmann, G. J. Kalman, Z. Donko, and K. Kutasi, Phys. Rev. E **72**, 026409 (2005).

[93] D. Dubin, Phys. Rev. Lett. **71**, 2753 (1993).

[94] J. Pieper, J. Goree, and R. Quinn, Phys. Rev. E **54**, 5636 (1996).

[95] M. Zuzic *et al.*, Phys. Rev. Lett. **85**, 4064 (2000).

[96] K. Strandburg, Rev. Mod. Phys. **60**, 161 (1988).

[97] H. Thomas and G. E. Morfill, Nature **379**, 806 (1996).

[98] R. A. Quinn *et al.*, Phys. Rev. E **53**, 2049 (1996).

[99] J. Pieper, J. Goree, and R. Quinn, J. Vac. Sci. Technol. A **14**, 519 (1996).

[100] V. A. Schweigert *et al.*, Phys. Rev. Lett. **80**, 5345 (1998).

[101] I. V. Schweigert *et al.*, JETP **87**, 905 (1998).

[102] I. V. Schweigert, V. A. Schweigert, A. Melzer, and A. Piel, JETP Lett. **71**, 58 (2000).

[103] I. V. Schweigert, V. A. Schweigert, A. Melzer, and A. Piel, Phys. Rev. E **62**, 1238 (2000).

[104] H. M. Lindsay and P. Chaikin, J. Chem. Phys. **76**, 3774 (1982).

[105] N. N. Rao, P. K. Shukla, and M. Y. Yu, Planet. Space Sci. **38**, 543 (1990).

[106] P. Shukla, Phys. Plasmas **8**, 1791 (2001).

[107] R. L. Merlino, A. Barkan, C. Thompson, and N. D'Angelo, Phys. Plasmas **5**, 1607 (1998).

[108] C. Thompson, A. Barkan, N. D'Angelo, and R. L. Merlino, Phys. Plasmas **4**, 2331 (1997).

[109] F. M. Peeters and X. Wu, Phys. Rev. A **35**, 3109 (1987).

[110] X. Wang, A. Bhattacharjee, and S. Hu, Phys. Rev. Lett. **86**, 2569 (2001).

[111] A. Homann, A. Melzer, R. Madani, and A. Piel, Phys. Lett. A **242**, 173 (1998).

[112] A. Homann *et al.*, Phys. Rev. E **56**, 7138 (1997).

[113] D. Samsonov *et al.*, Phys. Rev. Lett. **83**, 3649 (1999).

[114] D. Samsonov, J. Goree, H. Thomas, and G. Morfill, Phys. Rev. E **61**, 5557 (2000).

[115] A. Melzer, S. Nunomura, D. Samsonov, and J. Goree, Phys. Rev. E **62**, 4162 (2000).

[116] D. H. E. Dubin, Phys. Plasmas **7**, 3895 (2000).

[117] V. Nosenko, J. Goree, Z. W. Ma, and A. Piel, Phys. Rev. Lett. **88**, 135001 (2002).

[118] O. Havnes *et al.*, J. Geophys. Res. **100**, 1731 (1995).

[119] S. V. Vladimirov, P. V. Shevchenko, and N. F. Cramer, Phys. Rev. E **56**, 74 (1997).

[120] T. Misawa *et al.*, Phys. Rev. Lett. **86**, 1219 (2001).

[121] S. Nunomura *et al.*, Phys. Rev. Lett. **89**, 035001 (2002).

[122] B. Liu, K. Avinash, and J. Goree, Phys. Rev. Lett. **91**, 255003 (2003).

[123] S. Nunomura, S. Zdhanov, D. Samsonov, and G. E. Morfill, Phys. Rev. Lett. **94**, 045001 (2005).

[124] J. J. Thomson, Philos. Mag. **39**, 237 (1904).

[125] S. Neser, T. Palberg, C. Blechinger, and P. Leiderer, Prog. Colloid Polym. Sci. **104**, 194 (1997).

[126] *Nanostructure Physics and Fabrication*, edited by M. A. Reed and W. P. Kirk (Academic, Boston, 1989).

[127] P. Leiderer, W. Ebner, and V. B. Shikin, Surf. Sci. **113**, 405 (1982).

[128] V. M. Bedanov and F. Peeters, Phys. Rev. B **49**, 2667 (1994).

[129] Y.-J. Lai and L. I, Phys. Rev. E **60**, 4743 (1999).

[130] Y.-J. Lai and L. I, Phys. Rev. E **64**, 015601 (2001).

[131] W.-T. Juan *et al.*, Phys. Rev. E **58**, 6947 (1998).

[132] M. Klindworth, A. Melzer, A. Piel, and V. Schweigert, Phys. Rev. B **61**, 8404 (2000).

[133] Y. Ivanov and A. Melzer, Phys. Plasmas **12**, 072110 (2005).

[134] R. W. Hasse and V. V. Avilov, Phys. Rev. A **44**, 4506 (1991).